DESIGN OF A RECEIVER FOR MEASUREMENT OF REAL-TIME IONOSPHERIC REFLECTION HEIGHT

By

Raghavendar Changalvala

RECOMMENDED:

Denise Thorsen

Charles E Mayer

Advisory Committee Chair

Charles E Mayer

Chair, Department of Electrical and Computer Engineering

APPROVED:

Dean, College of Engineering and Mines

Susan M. Zemlicka

Dean of the Graduate School

August 4, 2005

Date

DESIGN OF A RECEIVER FOR MEASUREMENT OF REAL-TIME IONOSPHERIC REFLECTION HEIGHT

A

Thesis

Presented to the Faculty

of University of Alaska Fairbanks

in Partial Fulfillment of the Requirements

for the Degree of

MASTER OF SCIENCE

By

Changalvala Raghavendar, B.Tech.

Fairbanks, Alaska

August 2005

Abstract

The HF (high frequency) radar at Kodiak Island, Alaska, is part of the SuperDARN (Super Dual Auroral Radar Network) network of radars designed to detect echoes from ionospheric field-aligned density irregularities. Normal azimuth scans of the radar begin on whole minute boundaries leading to ~12 s downtime between each scan. The radar makes use of this down time, by stepping through eight different frequencies for each beam direction using 1 or 2 s integration periods. A new receiver system has been developed at Poker Flat Research Range (PFRR), to utilize the ground scatter returns from radar's sounding mode of operation and calculate the ionospheric virtual reflection height. This would result in considerable improvement in the accuracy of critical frequency and Angle Of Arrival (AOA) estimations made by the Kodiak SuperDARN.

Table of Contents

List of Figures

List of Tables

Chapter 1. Introduction

In recent years there has been an upsurge in the usage of the HF band for both civilian and military applications [1]. HF band communication systems depend on the ionospheric propagation conditions to a large extent. Hence, understanding and predicting the ionospheric propagation conditions in real-time is necessary. The virtual reflection height of the ionosphere is one of the critical factors to be considered while studying the ionospheric propagation conditions. This project designs a system which measures the virtual reflection height of the ionosphere by effectively using the down time of Kodiak Super Dual Auroral Radar Network (SuperDARN).

This chapter starts with a brief introduction to the effects of the ionosphere on radio wave propagation and explains various terms related to the ionospheric propagation of a radio wave. The motivation behind the project, the thesis problem statement, and the proposed solution of the design problem, are discussed in the end of the chapter.

1.1 Background

The ionized component of the atmosphere, composed of free electrons and positive ions in electrically neutral balance, is defined as the ionosphere. The ionosphere plays a basic role in long distance radio communications. The majority of the atmosphere at ionospheric altitudes is neutral, but the minority charged particles are responsible for long distance communications.

In 1902, Oliver Heaviside and Arthur E. Kennelly independently suggested the existence of a layer in the upper atmosphere that could account for the long-distance radio transmissions [2]. They confirmed the statements made the previous year by Guglielmo Marconi and others. Edward Appleton confirmed the existence of the Kennelly-Heaviside layer during the early 1920s and designated the electric waves that were apparently reflected from it with the letter E in his diagrams. In 1924, Appleton discovered two additional layers in the ionosphere, as he and Robert Watson-Watt named this atmospheric region, and noted them

with the letters D and F. Appleton was reluctant to alter this arbitrary nomenclature for fear of discovering yet other layers, so it has stuck to the present day. The basic physics of ionospheric propagation was largely worked out by the 1920s, yet both amateur and professional experimenters made further discoveries through the 1930s and 1940s.

The simplest way to visualize the ionosphere is to imagine a mirror situated between 100 and 400 km above the Earth's surface which allows reflected signals to reach points around the horizon of the Earth, as shown in Figure 1.1. This reflection in actual sense is refraction, which is gradual bending of the ray towards the horizontal as the refractive index of ionospheric medium decreases with an increase in the altitude [3]. Under suitable conditions, signals can propagate for thousands of kilometers. Reflection from the highest region (F region in general) provides largest range hop, but this depends on the ionospheric structure at that instant of time. High radio frequencies tend to reflect from greater heights, but at very high frequency the signal might penetrate through the ionosphere due to lack of sufficient bending. Also, for signals with low frequency and higher obliquity the absorption loss due to lower layers is larger [3]. Hence, radio communications generally require a compromise. The random nature of ionosphere makes communication difficult, but by understanding the basic mechanisms of ionosphere, efficient communication can be achieved.

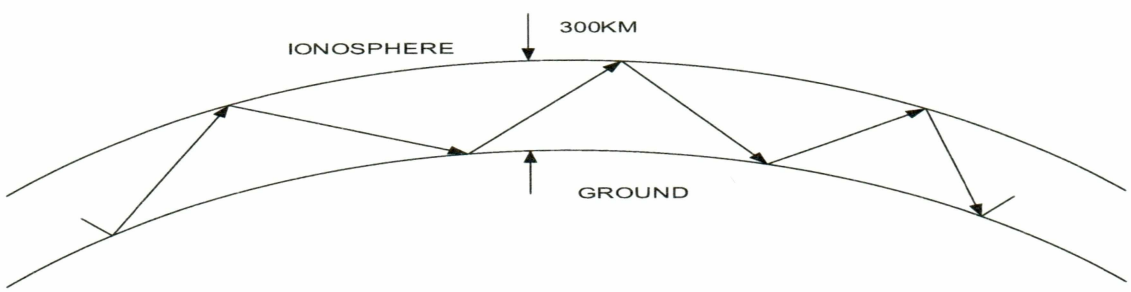

Figure 1.1 Long Distance Propagation by Multiple Hops between the Ionosphere and the Earth [3].

1.2 Structure of the Ionosphere

The vast research on the ionosphere since the 1930s has revealed many interesting facts about the ionosphere and its nature. The following paragraphs present a brief overview of the formation and composition of the ionosphere. The ionosphere extends from about 50 km above the surface of the Earth to roughly 650 km. It consists of several layers of ionization, which are formed primarily by a process called photoionization.

1.2.1 Photoionization

Photoionization occurs when ultraviolet photons from the sun impinge on the ionospheric region of the atmosphere, strike gas atoms and molecules, and knock electrons free. A normal atom is electrically neutral since it contains both a positively charged nucleus and negative orbiting electrons. When an electron is knocked free from the atom, the atom becomes positively charged (called a positive ion) and remains in space along with the free electron, which is negatively charged. This process is called ionization.

As the ultraviolet light continues to produce positive ions and negative electrons, its intensity decreases and an ionized layer is formed. The rate at which ionization occurs depends on the density of atoms and molecules in the atmosphere and the intensity of the ultraviolet light wave, which varies with the activity of the sun. Atmospheric composition variations with altitude cause variation of ionization and recombination rates, which results in a complex chemical balance yielding an ionospheric structure of multiple layers.

An important factor in determining the density of ionized layers is the elevation angle of the sun. For this reason, the height and thickness of the ionized layers vary depending on the time of day and even the season of the year.

1.2.2 Recombination

A reverse process to ionization, called recombination, occurs when the free electrons and positive ions collide with each other. In a collision, the electron is captured and the positive ions return to their original neutral atom state.

The balance between recombination and photoionization depends on the time of day. Between the hours of early morning and late afternoon, the rate of ionization exceeds the rate of recombination. During this period, the ionized layers reach their greatest density and exert maximum influence on radio waves. During the late afternoon and early evening hours, however, the rate of recombination exceeds the rate of ionization, and the density of the ionized layers begins to decrease. Throughout the night, density continues to decrease, reaching a low point just before sunrise.

1.2.3 Layers

Historically the ionosphere is divided into three regions, D, E, and F, which are in order of increasing altitude. These regions can be broken up into subregions under certain conditions, for example, as shown in Figure 1.2, where the F layer is further divided into two layers designated F1 (the lower layer) and F2 (the higher layer). From the viewpoint of HF propagation, the E and F regions act only as radio wave reflectors and permit long range propagation. The D region acts principally as an absorber, causing signal attenuation. The presence or absence of these layers in the ionosphere and their height above the Earth varies with the position of the sun as its radiation is the cause for ionization. While it is true that the level of ultra-violet (UV) radiation from the sun is not entirely predictable, the following general statements can be made about the ionosphere [4].

The D layer ranges from about 50 to 95 km and has plasma densities typically not more than $10^3/cm^3$. The D layer is the lowest region of the ionosphere. This layer has the ability to refract signals of low frequencies. High frequencies pass right through it and are attenuated. After sunset, the D layer disappears because of the rapid recombination of ions.

The E layer peaks at about 105 to 110 km and can have plasma densities as high as $10^5/cm^3$ or $10^6/cm^3$. This layer is also known as the Kennelly-Heaviside layer, because these two men were the first to propose its existence. The rate of ionic recombination in this layer is rather rapid after sunset and the layer decays rapidly when there is no source of ionization. This layer has the ability to refract signals as high as about 15 MHz in frequency. For this reason, it is valuable for communications for distances up to about 1500 miles.

The F layer exists from about 160 to 500 km and is typically the most dense layer of the ionosphere with densities of $10^5/cm^3$ or $10^6/cm^3$ or greater. During the daylight hours, the F layer separates into two layers, the F1 and F2 layers. The ionization level in these layers is quite high and varies widely during the day. At noon, this portion of the atmosphere is closest to the sun and the degree of ionization is at its maximum. Since the atmosphere is rarefied at these heights, recombination occurs slowly after sunset. Therefore, a fairly constant ionized layer can persist for many hours after sunset. The F layers are responsible for high-frequency (HF), long distance transmission.

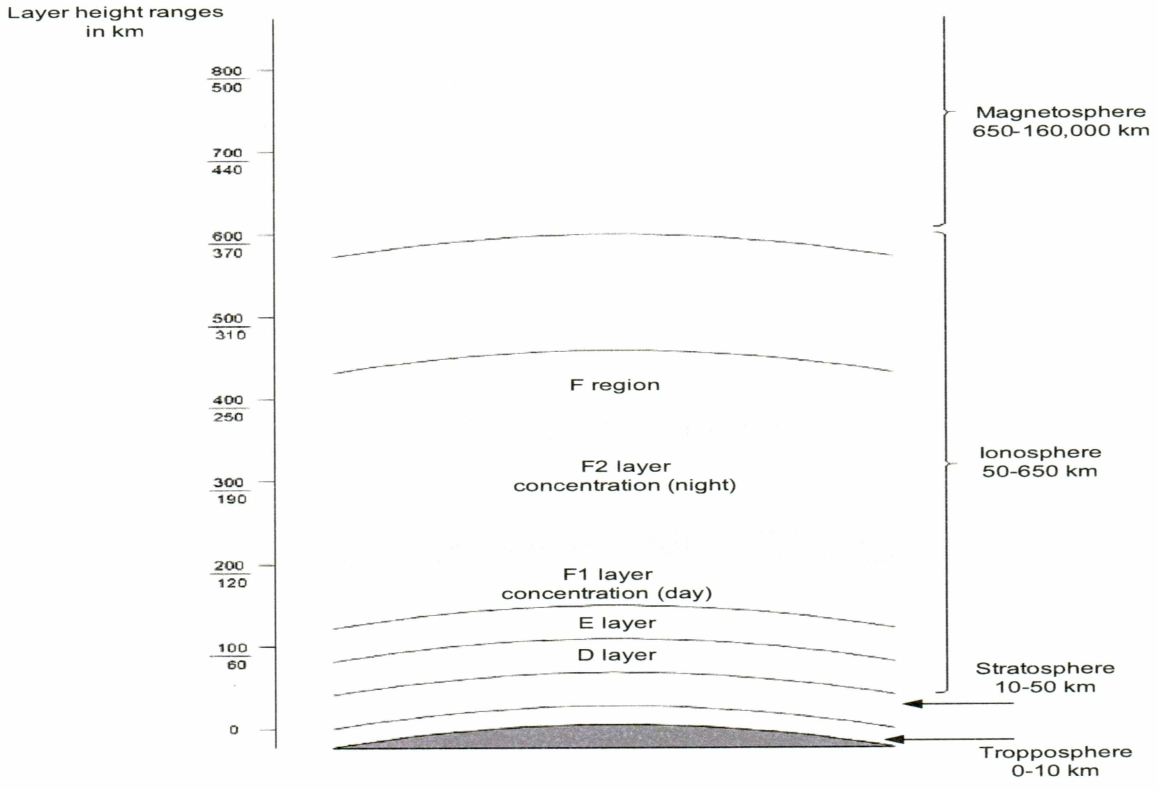

Figure 1.2 Above 50 km to about 650 km is the Ionosphere, Notable for Its Effects on Radio Wave Propagation [4].

1.3 Ionospheric Refraction

In general, the atmosphere shows a layered structure, with the refractive index, n, having a characteristic vertical profile but with much slower variation in the horizontal. For such a geometry of model atmospheres in which the refractive index is constant in curved shells as shown in Figure 1.3, Snell's law takes the form

$$n(R_E + h)\sin i = n_o R_E \sin i_o, \qquad (1)$$

where i is the angle of incidence of a ray on the shell at height h, and R_E is the radius of the Earth.

When a signal is transmitted into an ionized layer, refraction, or bending of the wave, occurs due to change in the velocity of a radio wave as it encounters a gradient of the index of refraction. This effect of the ionosphere on wave propagation is frequency dependent, as the ionosphere might be considered as a low conductivity dielectric with refractive index always less than unity, decreasing as electron density increases and frequency decreases [1].

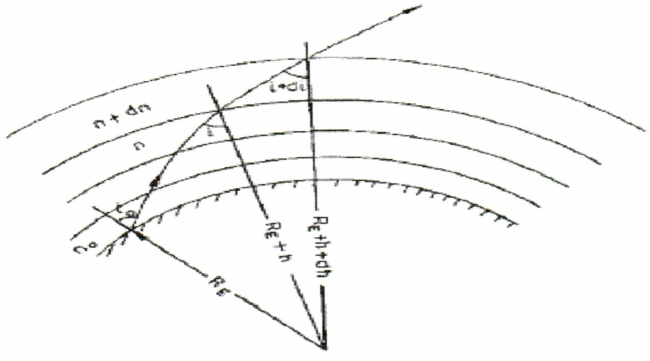

Figure 1.3 Geometry of Refraction of Radio Wave through the Stratified Ionosphere [1].

The amount of refraction that occurs depends on three main factors: (1) the density gradient of ionization of the layer, (2) the frequency of the radio wave, and (3) the angle at which the wave enters the layer.

HF rays below a certain **penetration** frequency, for a given launch angle, will be reflected back to the Earth. For any given point in the ionosphere, refraction is less for higher frequencies and for higher elevation angles. As the elevation angle is increased, the height of reflection is increased, reaching a maximum for vertical incidence. For low angles of elevation, the reflection path is long and the ground range from the transmitter is large [5]. The dependence of ionospheric rays on angle of incidence is depicted in Figure 1.4.

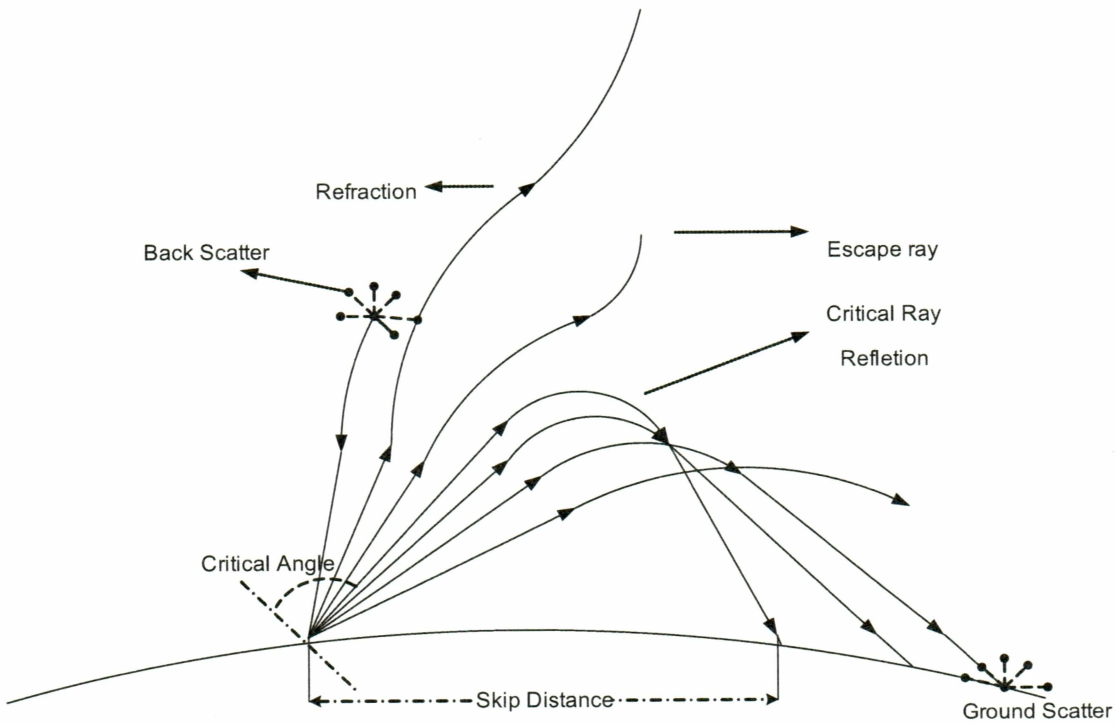

Figure 1.4 Dependence of Ionospheric Rays on Angle of Incidence [1].

If the frequency is increased, the height of reflection increases, and eventually, at the **critical frequency**, the ray will penetrate the ionospheric layer. This critical frequency is dependent on the maximum electron density of the layer. For frequencies below the critical frequency, rays transmitted with a zenith angle below a certain **critical angle** will be reflected back to ground. After being reflected, this critical angle ray reaches the ground at the so called **skip distance,** which is the minimum possible range for a given frequency. Some energy is scattered from the ground back along the tracks to the transmitter site, and some energy is scattered forward. In addition, some energy is scattered back from ionospheric irregularities, and some is absorbed. Figure 1.5 shows three separate waves of different frequencies entering an ionospheric layer at the same angle. Notice that the 5 MHz wave is refracted quite sharply. The 10 MHz wave is refracted less sharply and returned to Earth at a greater distance. The 15 MHz wave is obviously greater than the critical frequency for that ionized layer and, therefore, is not refracted but is passed into space [1].

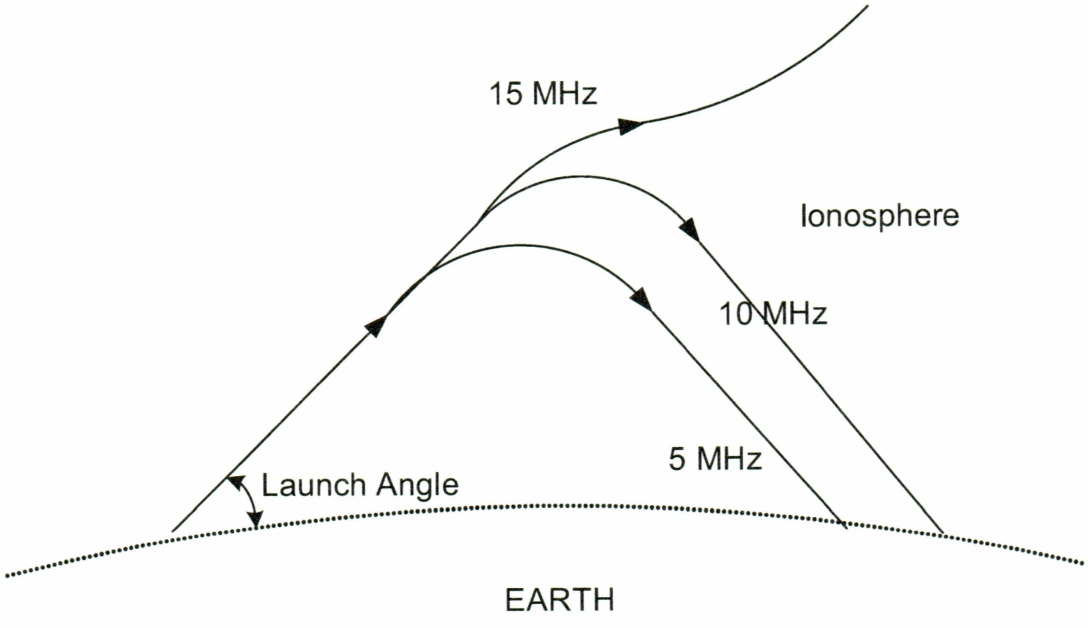

Figure 1.5 Frequency vs Refraction Distance.

For point to point transmission on the Earth's surface, there will be a **maximum usable frequency** (MUF), less than the penetration frequency and increasing with path distance. The MUF for any given transmission distance is calculated from the critical frequency by multiplying by the MUF factor, which is a function of transmission distance. This distance is associated with a certain angle of elevation of the transmitted wave. At the MUF, the ray path is that of the skip ray and, hence, the transmission distance is the minimum distance at which the ionospheric wave reaches the Earth again [1].

The absorption of an HF radio wave in the D region of the ionosphere is proportional to the inverse square of the frequency. The sensitivity of an HF receiver is usually limited by external noise which increases as the frequency reduces. Thus, there is a frequency limit below which the signal to noise ratio fails to reach an acceptable value for the service required. This is called **lowest usable frequency** (LUF).

The MUF and LUF depend on various factors like ionization density along the path in ionosphere, amount of UV radiation received, which in turn may depend on latitude, time of day, season of the year, and point in the 11-year sunspot cycle. They will also be affected by solar flares and bursts of streams of particles from sun causing ionospheric storms. Hence, to ensure a good communication link these factors should be monitored regularly [1].

1.4 Ionospheric Propagation

When a radio signal enters the ionosphere, its electric field imparts an oscillatory motion to the electrons. These electrons reradiate the wave like miniature antennas. This interaction with the electrons modifies the velocity of the propagation of the wave. The reradiated wave polarization in general differs from the incident wave polarization. Thus the resultant wave polarization changes continuously as the wave traverses the ionosphere. In its passage through the ionosphere, the signal imparts energy to each electron. The electron gives this energy back to the wave as it reradiates. If, however, the electron collides with another particle it loses energy, and the ordered energy supplied by the radio wave is converted into disordered energy and the wave is attenuated.

1.4.1 Reflection at Vertical Incidence

Neglecting the effects of the geo-magnetic field, the group velocity of a pulse entering ionospheric layer at vertical incidence from below is represented as

$$v_g = c\mu = c\sqrt{1-\left(\frac{Ne^2}{\pi m_e f^2}\right)}, \qquad (2)$$

where f is the wave frequency in Hz, N is number of electrons/unit volume, e is the electric charge = 1.602×10^{-19} coulombs, c is speed of EM wave in free space = 3×10^{8} m/s, m_e is the mass of the electron = 9.1×10^{-31} kg, and μ is the real part of the complex refractive index n [6].

From equation (2), we can deduce that as the pulse progresses vertically in the layer, the group velocity will decrease. If the layer electron density is sufficiently high, the wave of frequency f will eventually reach a point where the group velocity is reduced to zero and it will be reflected. The condition for vertical incidence reflection is n = 0, which can be written as

$$1-\frac{Ne^2}{\pi m_e f^2} = 0. \qquad (3)$$

The natural frequency of plasma oscillations due to thermal fluctuations is defined as plasma frequency, represented as

$$f_n = \frac{Ne^2}{\pi m}. \qquad (4)$$

From equation (2) and equation (4), the refractive index μ can be defined as

$$\mu = \sqrt{1 - \frac{f_n^2}{f^2}}. \qquad (5)$$

The condition for reflection of wave at vertical incidence can thus be defined as $f = f_n$, from equation (5).

1.4.2 Virtual Height Concept

The virtual height is the altitude from which a ray would have to reflect to give the same group delay as if it traveled with velocity c (3×10^8 m/s), throughout its path rather than at the actual speed as determined by the index of refraction. The refractive index of an ionospheric layer increases with the density of free-moving electrons, which usually peaks in the F region. Near the F region peak, the density gradient is graded so the radio waves are refracted gradually over a considerable vertical distance, usually amounting to tens of kilometers [3].

If we assume that a radio frequency (RF) pulse is propagating vertically upward at a speed accounting for variations of the index of refraction i.e., velocity of light in the medium, then the time required for this pulse to be reflected from an altitude h in the ionosphere and return to the Earth is given by

$$t = \frac{2}{c}\int_0^h dz / \mu. \qquad (6)$$

Using equation (5) and equation (6), the virtual height of reflection of pulse h' can be represented as

$$h'(f) = \frac{ct}{2} = \int_0^h \frac{dz}{\sqrt{1 - \frac{f_n^2}{f^2}}}. \qquad (7)$$

The virtual height mentioned in equation (7) is calculated on the assumption that the signal travels at the vacuum speed of light (3×10^8 m/s). In fact, as the pulse travels much slower at the same altitudes, the virtual height is always greater than the true height, which can be seen in Figure 1.6.

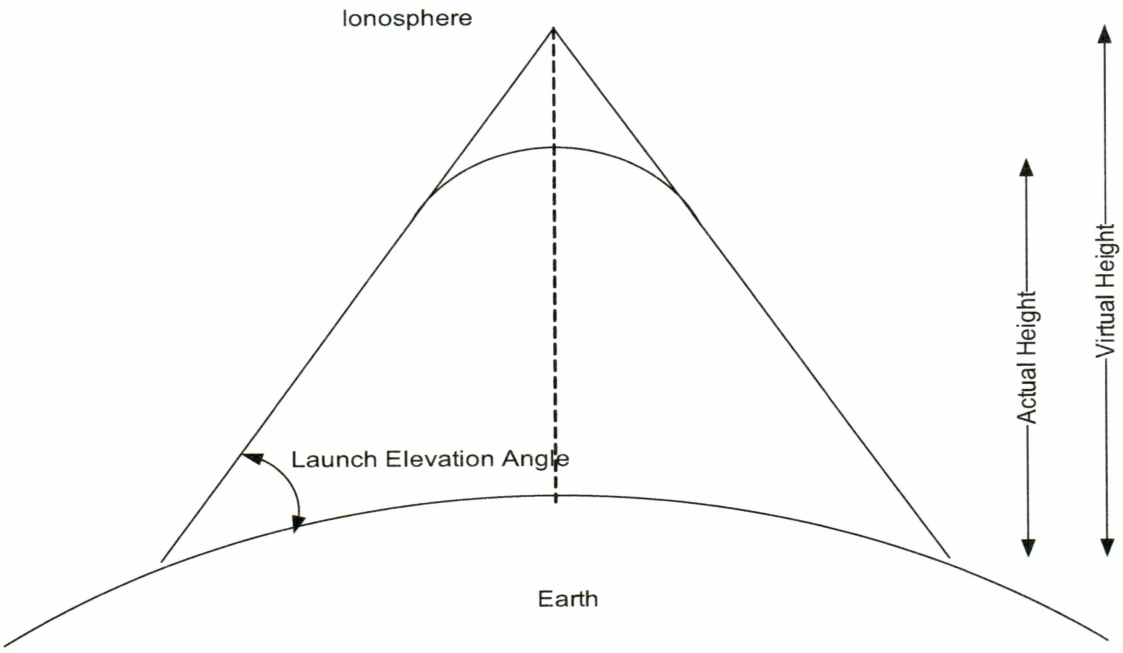

Figure 1.6 Figure Showing Difference between Actual and Virtual Reflection Heights.

1.4.3 Oblique Incidence

Again, if the effects of the Earth's magnetic field are ignored, then the refractive index n of the ionosphere is given by equation (5), which can be rewritten as

$$n^2 = 1 - \frac{f_n^2}{f^2}, \qquad (8)$$

where f is the wave frequency, and f_n is the plasma frequency, which is proportional to the square root of the electron concentration [3]. If, for simplicity, the ionization layer is considered to be divided into a number of thin strips of constant electron density, with each strip having a greater electron density than the one beneath it, then successive refraction at the boundaries between the strips will cause bending of the ray.

If successive slabs have refractive index of n_1 and n_2, then according to Snell's law the relation between angle of incidence ϕ_1 and angle of refraction ϕ_2 is

$$n_1 \sin\phi_1 = n_2 \sin\phi_2. \qquad (9)$$

Applying Snell's law at each boundary, if a ray enters the ionosphere at an angle of incidence ϕ_0, its angle to the normal of a slab with refractive index n_r is simply

$$\sin\phi_r = \frac{\sin\phi_0}{n_r}, \qquad (10)$$

and the ray will be reflected at a height where the ionization is such that n_r has the value

$$n_r = \sin\phi_0. \qquad (11)$$

This is the condition for reflection neglecting the magnetic field in the case of oblique incidence. The ray returns to the ground following the similar path. Here we notice that the process is bending, not reflection.

At vertical incidence, the reflection condition occurs when n equals zero and from equation (5) this occurs when $f = f_n$. If f_V represents the vertically incident frequency reflected at the level where plasma frequency is f_n, then for the obliquely incident wave

$$\sin^2 \phi_0 = 1 - \frac{f_n^2}{f^2} = 1 - \frac{f_V^2}{f_{ob}^2}. \qquad (12)$$

Hence, the secant law relating the vertical and oblique propagation could be stated as

$$f_{ob} = f_V \sec \phi_0, \qquad (13)$$

where f_{ob} and f_V are the frequencies of the signals reflected from the same true height, when f_{ob} is incident at an angle, and f_V is incident vertically. Thus, a frequency f_{ob} incident on the ionosphere at an angle ϕ_0 will be reflected from the same electron density as the equivalent vertical frequency $f_{ob} = f_V \sec \phi_0$ and, hence, a given ionospheric layer will always reflect higher frequencies at oblique incidence than at vertical incidence [3].

In order to determine the sec ϕ_0 and f_{ob} from vertical-incidence soundings (which measure the virtual height h') the results from Briett and Tuve's theorem are considered, which state that the time taken to traverse the actual curved path TABCR in Figure 1.7, at a given group velocity v_g, equals the time taken to travel over the straight line path TER at free space velocity, c (3×10^8 m/s) [3]. This could be expressed as

$$t = \int_{TABCR} \frac{ds}{v_g \sin \phi_0} = \frac{D}{c \sin \phi_0} = \frac{(TE + ER)}{c}. \qquad (14)$$

Also, Martyn's theorem states that if f_V and f_{ob} are the vertical and oblique frequencies respectively, reflected from the same true height h, then the virtual height at which the frequency f_{ob} is reflected equals the height of the equivalent triangular path for the frequency f_V. Referring to Figure 1.7, and defining equivalent path of oblique incidence for frequency f_{ob} as

$$p'_{ob} = 2TE, \tag{15}$$

we obtain

$$p'_V = \cos\phi_0 p'_{ob} = 2DE. \tag{16}$$

Hence, Martyn's theorem in concise form could be stated as

$$h'_{ob} = h'_v. \tag{17}$$

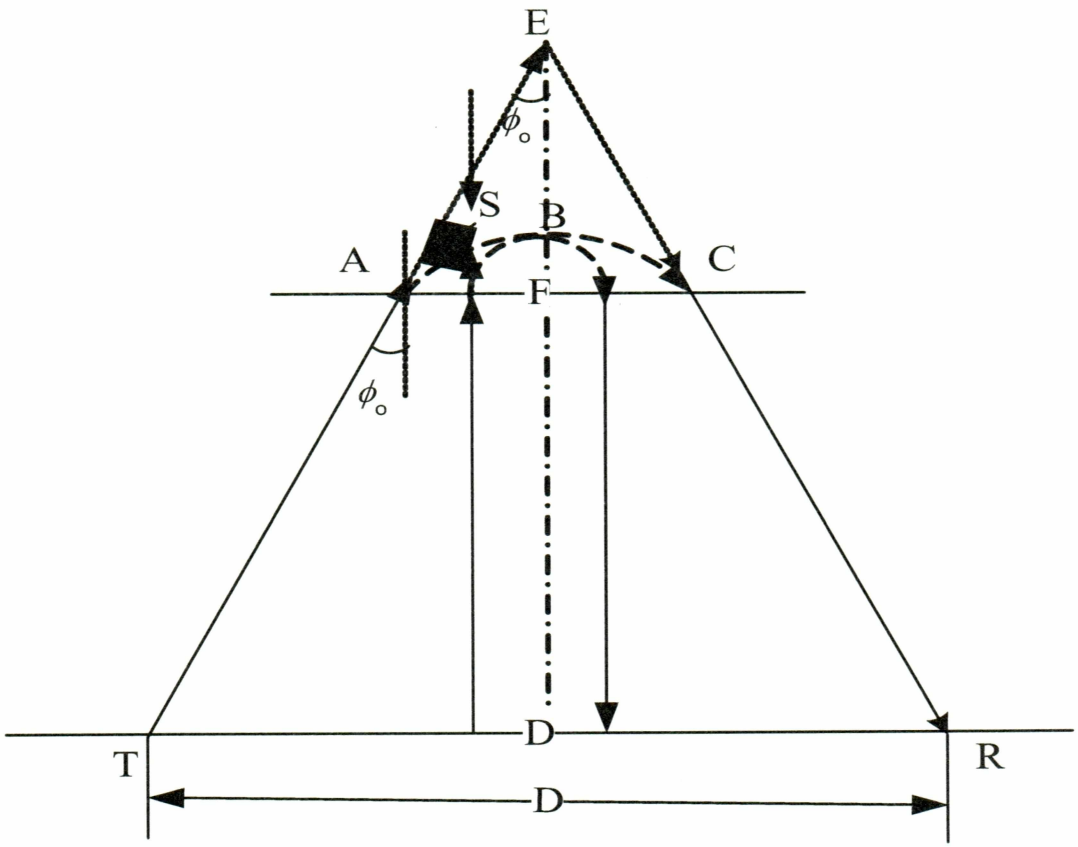

Figure 1.7 The Geometry Describing the Vertical and Oblique Ionospheric Propagation [6].

1.5 Motivation

HF communication systems find many applications in long range communications. At HF there are multiple sub-bands for different services, with many being shared among services. Of the 28 MHz available spectrum, approximately 55% is occupied by fixed services, 15% by land and maritime mobile services, 15% by sound broadcasting services, 10% by aeronautical mobile services, and the remaining 5% by amateur services. Currently, there is an upsurge in the use of HF band, both for civilian and military applications. Particularly for the military purposes, HF systems serve as back-up to fixed links established by other means.

These communication systems are strongly affected by the space weather fluctuations because the state of ionospheric medium through which they propagate is continually changing in response to space weather conditions. Ionospheric effects of space weather can include sudden changes in spatial structure and density of D, E, and F regions. These changes alter the MUF on which the HF communication systems depend [1].

Hence, a real-time estimation of ionospheric propagation conditions like MUF and ionospheric critical frequencies is significant in space weather monitoring. Estimation of the virtual reflection height of the ionosphere at various frequencies would help us in determining the critical propagation conditions. This motivated me to develop a system which would estimate the ionospheric virtual reflection height in real-time, using Kodiak SuperDARN.

1.6 Problem Statement and Proposed Solution

Briefly stated, the thesis problem was to design a system that measures the virtual reflection height of the ionosphere by effectively using the down time of Kodiak SuperDARN radar network.

A basic design approach was to let the transmitter transmit signals into the ionosphere and build a receiver at a fixed distance from the transmitter to receive the signals that are reflected from the ionosphere. Finding the time of transmission of the signal and assuming signal travels with the velocity of light (3×10^8 m/s) throughout its path, the virtual reflection

height of the ionosphere could be calculated using simple geometry as shown in Figure 1.8. Looking at Figure 1.8, if we assume that the transmitter and receiver are located at T and R respectively, then the distance of separation TR is a known parameter. Once we calculate the time of transmission of signal, the distance TER could be calculated by using the relation

$$TER = ct, \tag{18}$$

where TER is the total distance traveled by the signal in time t, and c is the velocity of light in vacuum (3×10^8 m/s). Once we determine the value of TER, as we know TR, using the relation

$$ED = \sqrt{ET^2 - TD^2}, \tag{19}$$

the virtual reflection height ED can be determined.

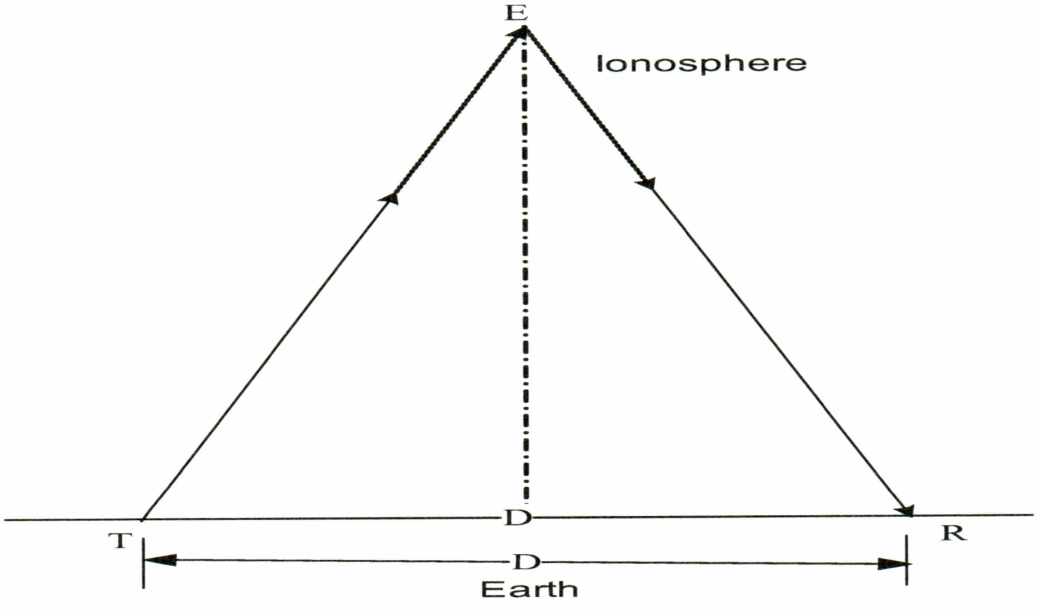

Figure 1.8 Diagram Showing the Applied Geometry to Measure the Reflection Height.

The actual design implementation was based on the simple concept stated above. The Kodiak SuperDARN radar network was used as the transmitter, and a receiving module was built in Poker Flat Research Range (PFRR), which is located at a distance of 877 km from Kodiak SuperDARN. Both the transmitter and receiver were synchronized using Global Positioning System (GPS) timers, and the time of transmission and the virtual reflection height were determined. There were many fixed parameters like transmitter location and its operating modes, location of the receiver antenna, the operating system, and the receiver card, which made the design task more interesting and challenging.

The forthcoming chapters are structured in a way to provide a detailed description of the steps implemented to attain the final result. Chapter 2 explains the specifications of the important equipment used in the receiver system design. The actual system design and configuration along with the signal processing and reflection height calculations are dealt with in Chapter 3. The final results and suggestions for future work are mentioned in the final chapter.

Chapter 2. Equipment Overview

This chapter aims at explaining the specifications of the important equipment used in the design of a receiver system to measure the virtual reflection height of the ionosphere. As the system uses the Kodiak SuperDARN radar network as the transmitter, this chapter starts with a brief description of the radar concepts, followed by a brief description of Kodiak SuperDARN radar's location, properties, and operating modes. Also, the receiver antenna construction parameters and design analysis are presented. The chapter ends with the descriptions of the receiver card and the clock card, which constitute the other important components of the design.

2.1 Basic Radar Definitions

In simple terms, radar could be considered as a device that radiates electromagnetic energy and detects targets by examining the reflected energy from them [7]. A simple radar schematic is shown in Figure 2.1. The term target is applied to any reflecting object, which interferes with the transmitted wave and reflects part of its energy.

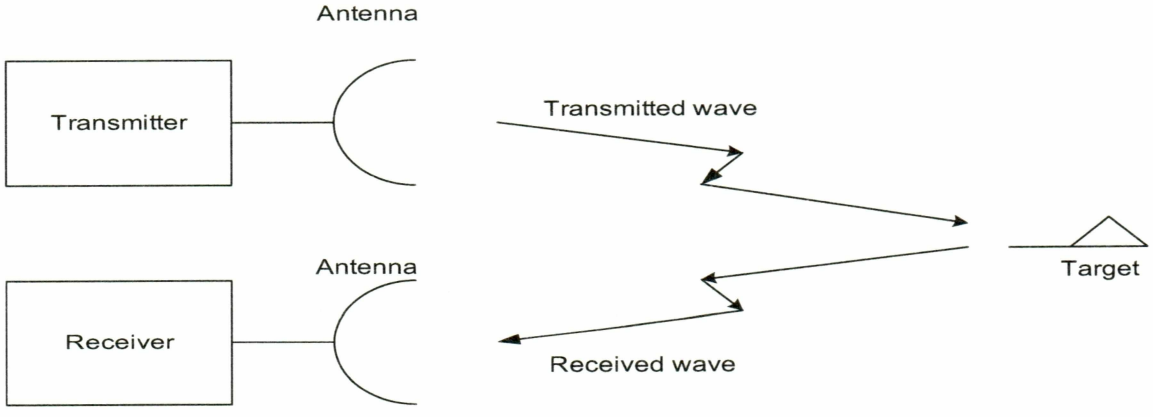

Figure 2.1 Radar Set Utilizing Separate Transmit and Receive Antennas [7].

Basic operation of a radar transmitter is explained in Figure 2.2. The transmitter primarily consists of an oscillator generating electromagnetic energy at a certain frequency, say ω_o, and a pulse generator that generates pulse trains, which are used to modulate a power amplifier [8]. The transmitted signal is a pulsed sine wave as shown in Figure 2.2. If we assume that the transmit and receive antennas are same, then the received energy from a target intercepted from a particular pulse will have a time delay of

$$\Delta t = \frac{2R}{c_m}, \tag{20}$$

where R is the true distance from the antenna to the target and c_m is the velocity of light in the given medium. The maximum unambiguous range as a function of pulse period is given by

$$R_{\max} = \frac{c_m T_r}{2} = \frac{c_m}{2 f_r}, \tag{21}$$

where f_r is the frequency of the pulse being transmitted.

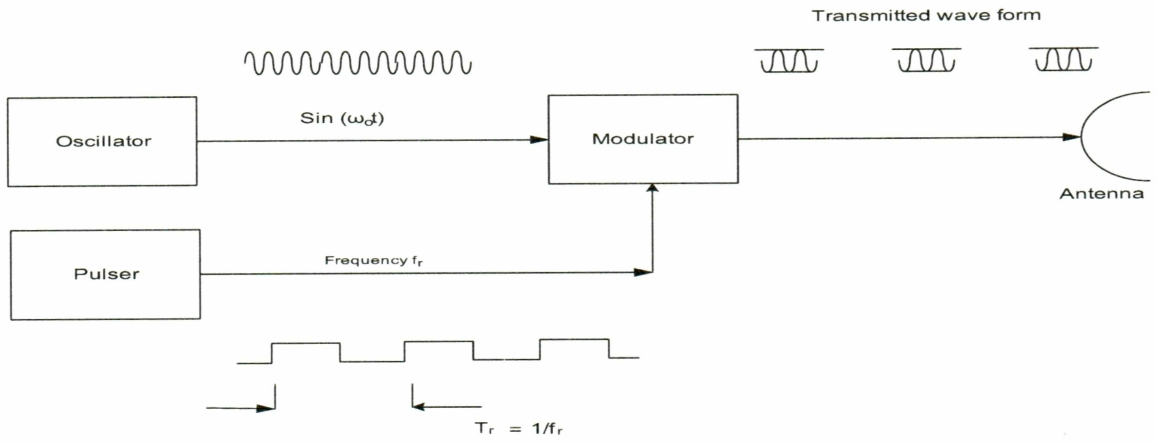

Figure 2.2 Radar Transmission of a Pulse Waveform [8].

2.2 Overview of the HF Radar at Kodiak

There are fifteen radars in the SuperDARN network, which are operated by ten different institutions around the world. The Geophysical Institute at the University of Alaska Fairbanks operates the radar located near Chiniak, Alaska, on Kodiak Island. This radar is known throughout the SuperDARN community as the radar at Kodiak and will be referred to as such within this thesis [9].

The HF radar at Kodiak consists of sixteen log-periodic antennas in the main array, four antennas in the interferometry array, sixteen 600 W transmitters, two synthesizers, a receiver, phasing electronics, and two control and processing computers.

The main antenna array is a linear array consisting of sixteen log-periodic antennas separated by 15.24 meters. Time delay phasing is implemented to steer the main beam of this array over ± 26° off perpendicular in 16 discrete increments. The typical field of view of the radar, along with some typical data, is shown in Figure 2.3.

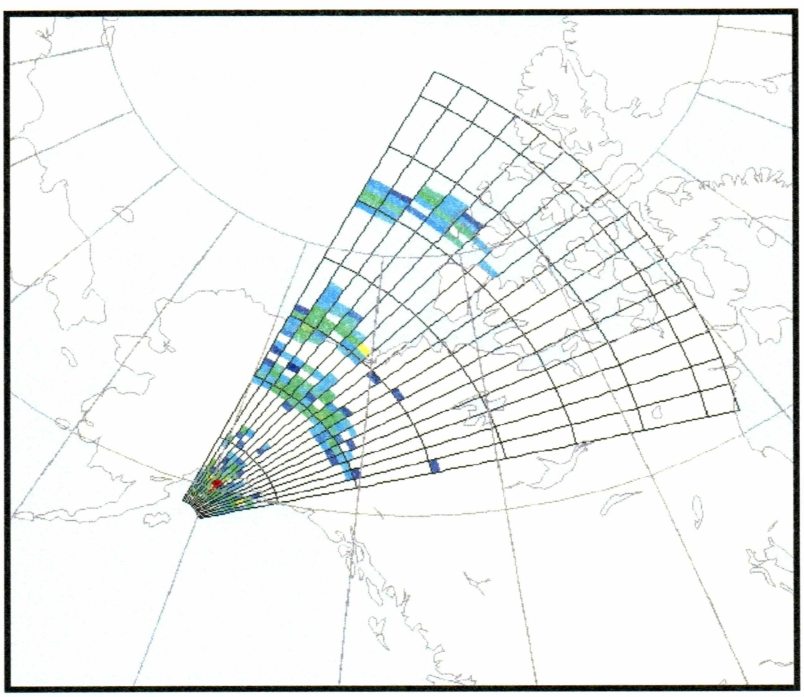

Figure 2.3 Typical Field of View for the HF Radar on Kodiak Island [9].

Figure 2.3 shows data from a typical operating mode. Each line in range represents ten 45 km range gates, or 450 km, starting at the first range of 180 km. Each line in azimuth bounds one of the 16 discrete beam directions.

Typically, data are collected for ranges from 180 km to 3555 km distance from the radar. One-hundred meters behind the main array is a second array of four antennas. The main array and the secondary array form a one-dimensional interferometer. Time delay phasing is also used in the interferometry array to estimate the vertical angle of arrival of the received signals. The beams of both arrays are synchronized so that the main beams of both arrays are always pointing in the same direction [9].

Control and data processing hardware is placed in a shelter located between main array and inferometery array. Two computers control the system. One is used solely to control the precise timing signals for the radar functions. The other is used to host the radar control programs, to sample the baseband signal, and to do all of the data processing, collection, and storage. The shelter also contains the phasing matrix, the signal generators, the mixers, and the receiver. A photograph of the radar site at Kodiak Island is provided in Figure 2.4.

Figure 2.4 Photograph of the HF Radar Site on Kodiak Island [9].

The photograph shows the sixteen log-periodic antennas that constitute the main array of the radar, the four antennas of the interferometry array, and the shelter housing most of the radar hardware.

The SuperDARN HF radar at Kodiak is very similar in design to most of the other radars in the network. While a detailed discussion of the design and implementation of this radar system is beyond the scope of this thesis, a brief discussion will be presented [9].

2.2.1 Frequency of Operation

The radar at Kodiak is designed to scatter signals from field-aligned electron density irregularities drifting with the plasma of the ionosphere. In order to receive the scatter, the incident wave must be nearly orthogonal to the magnetic field lines along which the irregularities form. At high latitudes, refraction of the incident radar signal is required to achieve orthogonality. Refraction of electromagnetic waves requires that the frequency be close to the ionospheric plasma frequency. The radars in the SuperDARN network have a wide frequency band over which they can operate to maximize the scatter from the field-aligned irregularities under a wide variety of ionospheric conditions. Each of the radars is designed to operate from 8 to 20 MHz. Since the propagation conditions in the ionosphere are highly variable, and propagation path of an electromagnetic wave within the ionosphere is a function of the frequency of the wave, this wide operating band maximizes the likelihood that some field-aligned irregularities are observable.

Not all the frequencies within 8 to 20 MHz band are available for usage. The FCC license that governs the frequencies at which the radar can transmit permits operation on 15 bands within the operating range of 8 to 20 MHz. In normal operation, one of the frequency bands is chosen to maximize the probability of observing ionospheric scatter. Once the frequency band is fixed, the system searches for a clear frequency, which is the frequency with the lowest received noise power, within a given band. Depending on the operating mode, a new frequency is typically chosen every 3 to 6 s. During clear frequency search, within a given band the radar can select any discrete frequency that is a multiple of the characteristic

incremental frequency of that band. The incremental frequencies vary from 300 Hz to 8 kHz for different bands.

The FCC license also dictates the bandwidth of the transmitted signal. The current license limits the signal bandwidth to 22 kHz, which limits the operating potential of the radar. This puts practical limits on the pulse width and modulation bandwidth, which limits the achievable range resolution of the radar.

2.2.2 Sounding Mode

At SuperDARN sites, in normal operating mode the azimuth scans are forced to begin on a integer minute boundaries. Stepping through the sixteen beam azimuths with a 3 s dwell time in each direction requires 48 s. This results in ~10 s per minute downtime when no data are collected. A new mode called **sounding mode** was developed which utilizes the ~10 s downtime to collect some useful data, in addition to the normal scan. In sounding mode, the radar fills the down time by taking additional observations at certain fixed frequencies, spaced between 10 and 19 MHz, which are listed in Table 2.1.

Table 2.1 Sounding Mode Frequencies.

Sounding Mode Frequency Table							
10.4 MHz	11.4 MHz	12.05 MHz	14.4 MHz	15.4 MHz	15.6 MHz	16MHz	18.2 MHz

During the time available between the azimuth scans, the sounding mode steps through this frequency table for each beam direction using a 1 s integration period. Since only 10 s are available, a full scan at each frequency can be obtained only after a number of azimuth scans.

At each of the frequencies mentioned above, a clear frequency search is carried out within a bandwidth of 200 kHz, to find a frequency with the lowest received noise power. Then the radar transmits at that clear frequency.

2.2.3 Antennas

The antennas used at the Kodiak HF radar are model 608 log-periodic antennas manufactured by Sabre Communications Corporation. These antennas are specified for use over the band of 8 to 20 MHz. Sabre specifies a forward gain of at least 12 dBi for 8 to 15 MHz, and of at least 14 dBi for 15 to 20 MHz. The front-to-back ratio is specified at 14 dB averaged over the band. The voltage standing wave ratio (VSWR) is less than 2.0 over the band. The plot of VSWR, constructed from specifications provided by the manufacturer, is shown in Figure 2.5.

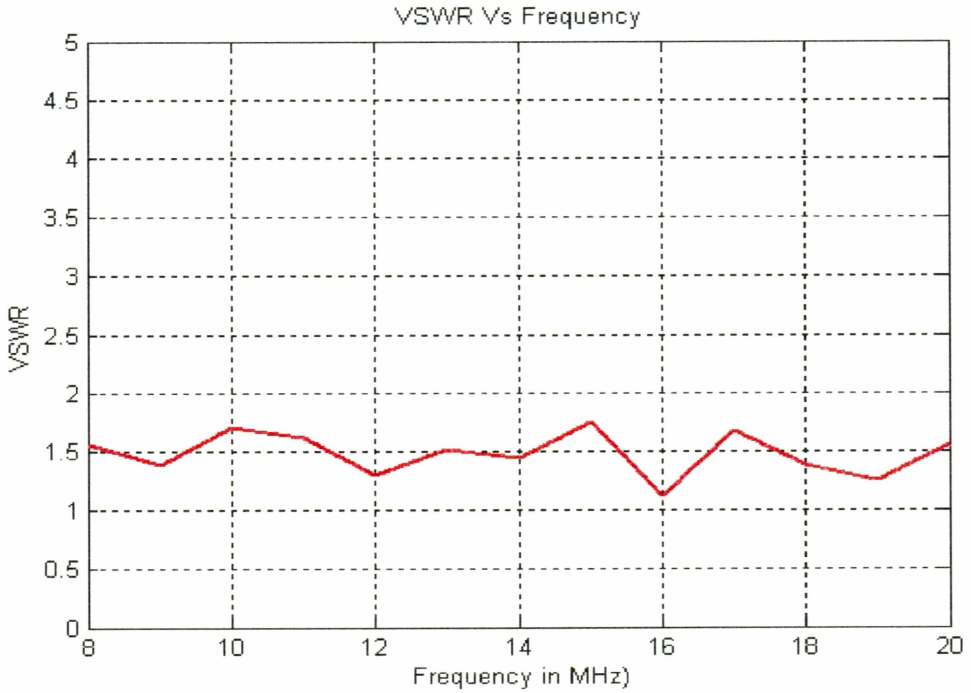

Figure 2.5 VSWR of Log-Periodic Antenna over the Frequency Band.

A numerical electromagnetic code (NEC) model of the antenna yields a pattern consistent with the specifications of the antenna [9]. Modeling the radiating structure in a NEC software package called EZNEC yields the azimuthal radiation pattern shown in Figure 2.6.

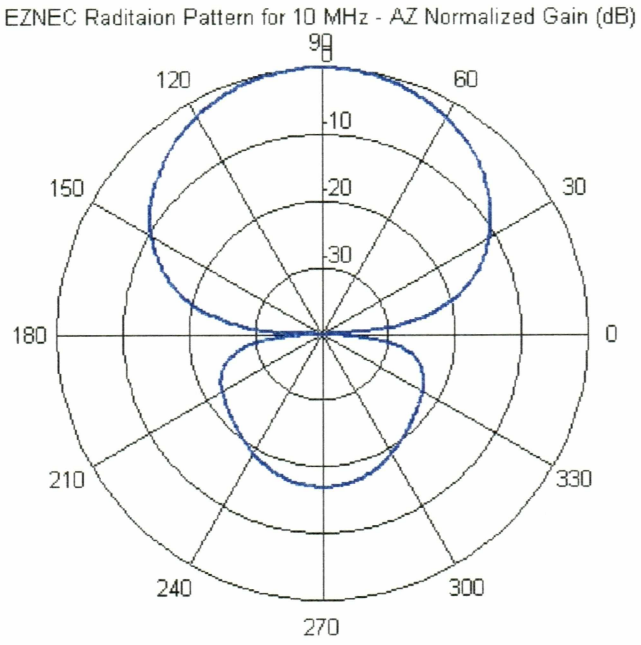

Figure 2.6 Normalized Azimuthal Radiation Pattern of a Single Antenna at the Kodiak HF Radar at 10 MHz.

The plot of the azimuthal radiation pattern is normalized and the angles are referenced to the line of the array. Ninety degrees is the forward-looking direction. The gain of the antenna at the shown frequency of 10 MHz is 13.4 dBi. The front-to-back ratio is 16.8 dB.

Similarly, the elevation radiation pattern for the log-periodic antenna 50 ft above a ground plane is shown in Figure 2.7.

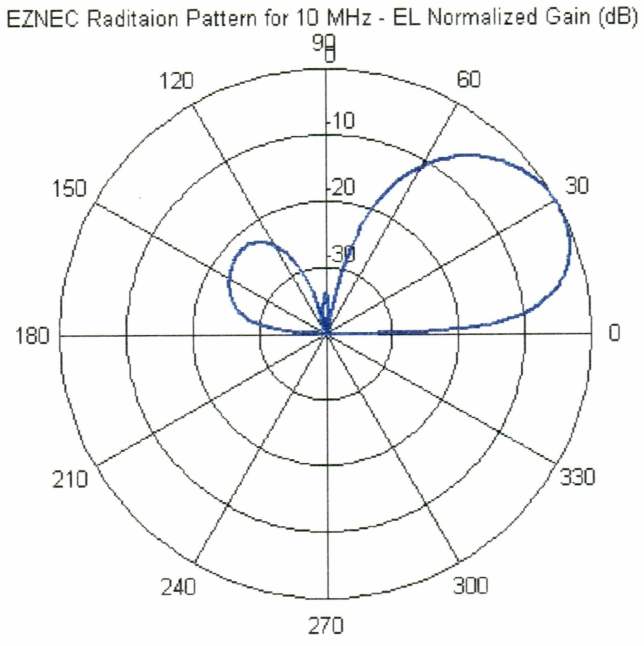

Figure 2.7 Normalized Elevation Radiation Pattern of the Main Array at 10 MHz with a Ground Plane.

Here, the peak of the main lobe is at 27° above the horizon, with a 3 dB beam width of 30.7°. The geometry, with this main lobe peak angle, is ideal for probing the upper atmosphere. As per the manufacturer specifications, this antenna should have very good radiating properties for the application of the HF radar at Kodiak. It should be noted, however, that these radiation patterns have not been experimentally verified at the radar site.

The HF radar at Kodiak implements the Sabre Communications Corp. Model 608 log-periodic antennas in two linear arrays. One of the arrays, the main array, consists of 16

antennas. This array is used for both transmission and reception. The second array, which is the interferometry array, consists of 4 antennas and is used only for reception.

The antennas in both arrays are positioned atop 50 ft towers, and are spaced 50 ft apart. A top view of the array geometry is provided in Figure 2.8.

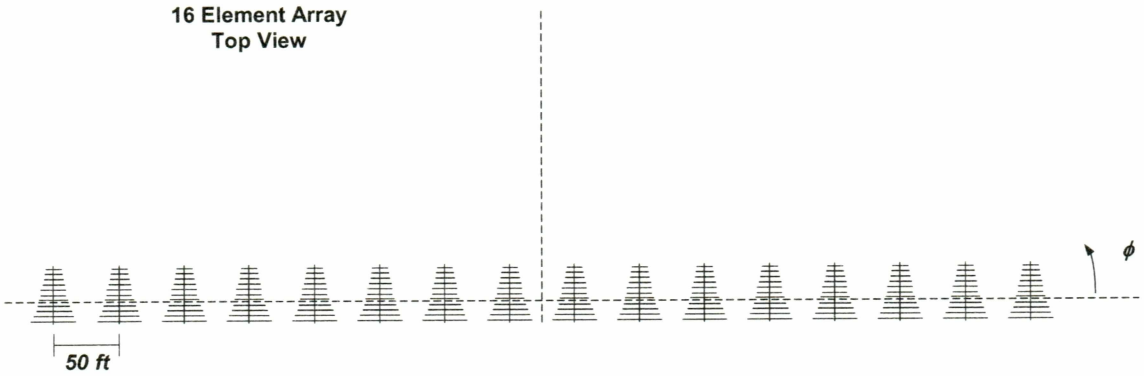

Figure 2.8 Top View of the Main Array Geometry [9].

The array acts to increase the radiative gain of the system and allows electronic steering of the beam. Using equations developed in [10], the azimuthal pattern of the array can be determined for various feed phase delays. The equation describing the normalized azimuthal pattern of the array is given as

$$E = \frac{1}{n}\frac{\sin(n\psi/2)}{\sin(\psi/2)}, \qquad (22)$$

where n is the number of elements in the array (16 for SuperDARN main array) and ψ is the phasing, given by,

$$\psi = d_r \cos(\phi) - \delta. \qquad (23)$$

In equation (23), d_r is the element spacing in radians ($d_r = 2\pi d/\lambda$), where λ is the wavelength of the transmitted signal, and δ is the introduced phase delay.

Using the properties of arrays as described by [10] the gain of the array can be calculated. The relation that the maximum possible electric field, E_{max}, from an array is equal to the number of elements, n, in the array times the electric field, E_0, due to one of the elements in the array is represented as

$$E_{max} = nE_0. \qquad (24)$$

Since the radiated power is directly proportional to the square of the electric field, equation (24) can be written in terms of power as

$$P_{max} = n^2 P_0, \qquad (25)$$

where P_0 is the power radiated from a single antenna. This means the peak gain due to the array is $n^2 = 16^2 = 256$. This gives a gain of 24.1 dBi due to the array. Since each antenna is rated at a minimum of 12 dBi over the band of operation, the total gain, G_{total}, of the main antenna array is

$$G_{total} = 12 + 10\log(256) = 36.1 \text{ dBi}. \qquad (26)$$

Taking equations (22) and (23) and setting the introduced phase delay between elements in the array, δ, to zero, the radiation pattern due to the array can be determined. The azimuthal radiation pattern due to the array is shown in Figure 2.9.

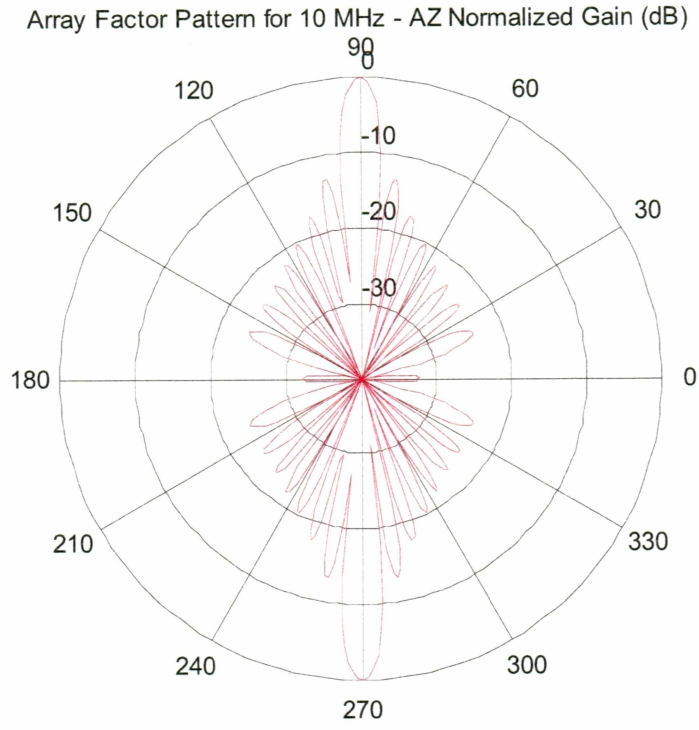

Figure 2.9 Normalized Azimuthal Array Pattern for the Main Array at 10 MHz [9].

Figure 2.9 shows that there are a large backlobe and significant sidelobes in the array pattern. The backlobe, however, is drastically reduced when the 16.8 dB front-to-back ratio of the antenna is considered. This is evident when the total radiation pattern, which is the product of the antenna pattern and the array factor, is examined [9]. The total azimuthal radiation pattern of the main array is shown in Figure 2.10.

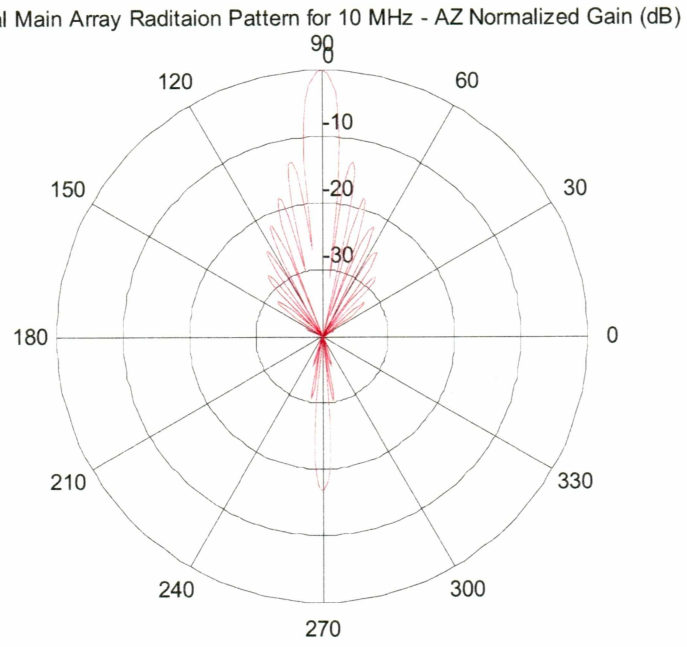

Figure 2.10 Normalized Azimuthal Total Radiation Pattern for the Main Array at 10 MHz [9].

2.2.4 Power

The HF radar at Kodiak has 16 transmitters associated with its 16 antennas. Each transmitter is rated for 600 W of transmitted power for a total transmit peak power of 9600 W. In typical operation, there are about 70 pulses transmitted per second. Given the typical pulse width of 300 μs, the average transmitted power is 201.6 W. With a total gain of 36.1 dBi, the effective radiated power (ERP), of the main array is

$$ERP = G_{total} + P_0, \qquad (27)$$

where G_{total} is specified in dBi and P_0 is given in dBW. Taking G_{total} as 36.1 dBi, and P_0 as 600 W = 27.8 dBW, the effective radiated power is 63.9 dBW or 2.44 MW. So, for an average

transmitted power of only 201.6 W, an effective radiated peak power of 2.44 MW is achieved [9].

2.3 Receiver Antenna

An open wire square biconical corner reflector antenna constructed at PFRR was used as receiving antenna in this project. The following paragraphs briefly analyze the reflector concept and then discuss the performance of the constructed antenna.

2.3.1 Reflector Analysis

Considering a simple case, two flat reflecting sheets intersecting at corner angle form a good directional antenna called corner reflector [11]. The corner reflector antenna can be easily analyzed using the method of images and array theory. If we consider a 90° corner reflector antenna as shown in Figure 2.11, then according to the method of images, the three images #2, #3 and #4 contribute to the field pattern of single source #1.

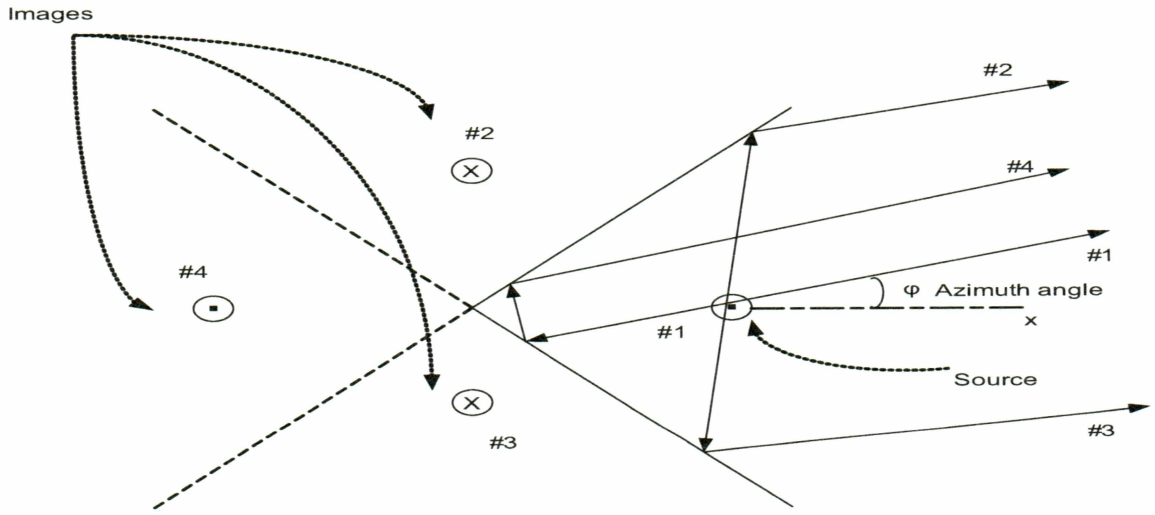

Figure 2.11 Right Angle Corner Reflector with Images Shown and How They Account for the Reflection [11].

The array factor contributions of the images shown in Figure 2.11 can be derived using the array theory. Considering a simple case of one image and one source, the array factor contribution from source element #1 and image element #4 can be derived easily using Figure 2.12.

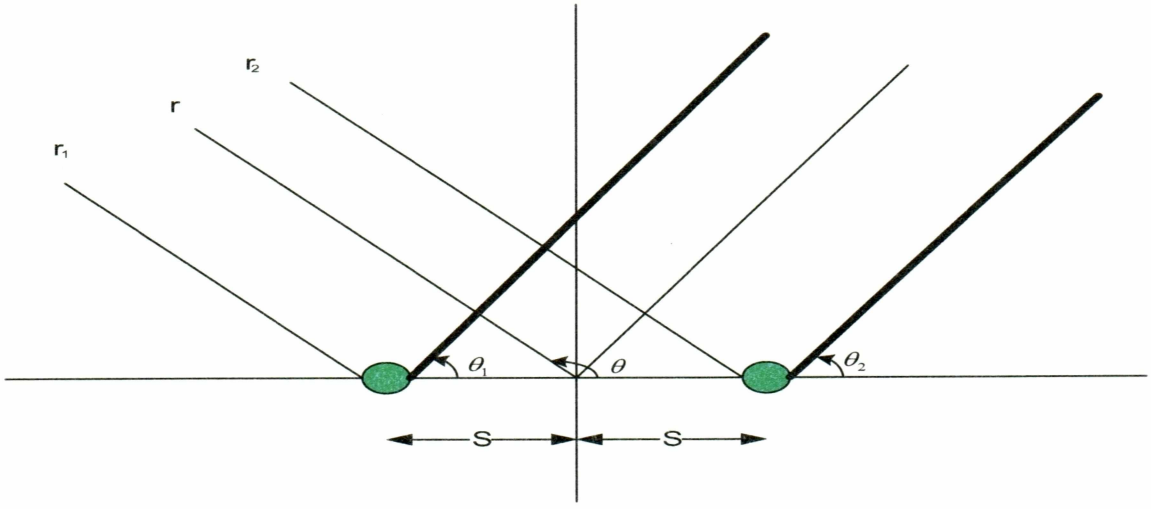

Figure 2.12 Figure Showing the Array Factor Contribution of Two Antenna Elements [11].

Figure 2.12 shows two dipoles separated by a distance of 2S. The currents in these dipoles are equal in magnitude but have a phase difference of β. If we consider one of them to be the source #1, and other to be its image #4, then the electric field in the far field region can be expressed as [11]

$$\overline{E_t} = \hat{\theta} j\eta \frac{kI_0 l}{4\pi}\left[\frac{e^{-j(kr_1-\beta/2)}}{r_1}\sin\theta_1 + \frac{e^{-j(kr_2-\beta/2)}}{r_2}\sin\theta_2\right], \qquad (28)$$

where k is the wave number, l is the length of the dipole, η is intrinsic impedance, and I_0 is the current magnitude. To represent equation (28) in a simple form [11], the distances r_1 and r_2 can be approximated to r in the denominator, but more accurate approximations are required in the phase terms namely, $r_1 = r - S\cos\theta$ and $r_2 = r + S\cos\theta$. Substituting these approximations, equation (28) reduces to the form

$$\overline{E_t} \cong \left[\hat{\theta} j\eta \frac{kI_0 l e^{-jkr}}{4\pi r}\sin\theta\right] 2\cos[(kS\cos\theta + \beta)/2]. \qquad (29)$$

In equation (29), the item in the first bracket on the right hand side is the element pattern of a single electric dipole, and the second item is the array factor [11]. The array factor of the two elements can be calculated exactly using Figure 2.12. If we use phases corresponding to the path length differences shown in Figure 2.12, the array factor becomes

$$AF = 1\times e^{-j\beta S\cos\theta} + 1\times e^{j\beta S\cos\theta} = 2\cos(\beta S\cos\theta), \qquad (30)$$

where S is the antenna-to-corner spacing. Looking at Figure 2.11, the array factor contribution from images #2 and #3 will be similar to the contribution due to #1 and #4, shown in equation (30), but out of phase and rotated by 90°, i.e., $-2\cos[\beta S\cos(90^\circ-\phi)]$. Thus, if we assume that the conducting and reflecting sheets are infinite in extent, the array factor in the xy-plane (H-plane) valid in the region $-45^0 \le \phi \le 45^0$ is

$$AF(\theta = 90^\circ, \phi) = 2\cos(\beta S\cos\phi) - 2\cos(\beta S\sin\phi), \qquad (31)$$

and in xz-plane (E-plane) is

$$AF(\theta, \phi = 0) = \{-2 + 2\cos[(\beta S\cos(90-\theta)]\}g(\theta). \qquad (32)$$

From equation (31) and equation (32) the pattern shape is a function of both the azimuth angle ϕ and antenna-to-corner spacing S, the values of which were carefully selected while constructing the antenna.

Often a Brown-Woodward dipole (bow-tie) is used as feed instead of an ordinary dipole, as it has superior impedance and bandwidth properties. In our project we used an open wire square biconical dipole antenna, for ease of construction. In the above analysis it is assumed that reflectors are perfectly conducting and of infinite length, which is the ideal case. For practical purposes we need a conducting plate of finite length. Looking at Figure 2.13, one can determine that L = 2S is the reasonable minimum length of the reflector, where S is the antenna-to-corner spacing. Only the waves that are radiated in sectors η are reflecting from infinite sides beyond B, and these waves are reflected with infinite sides in a direction that is at a considerable angle ϕ with respect to the axis. Hence, absence of reflector beyond B should not have a large effect on the radiation pattern.

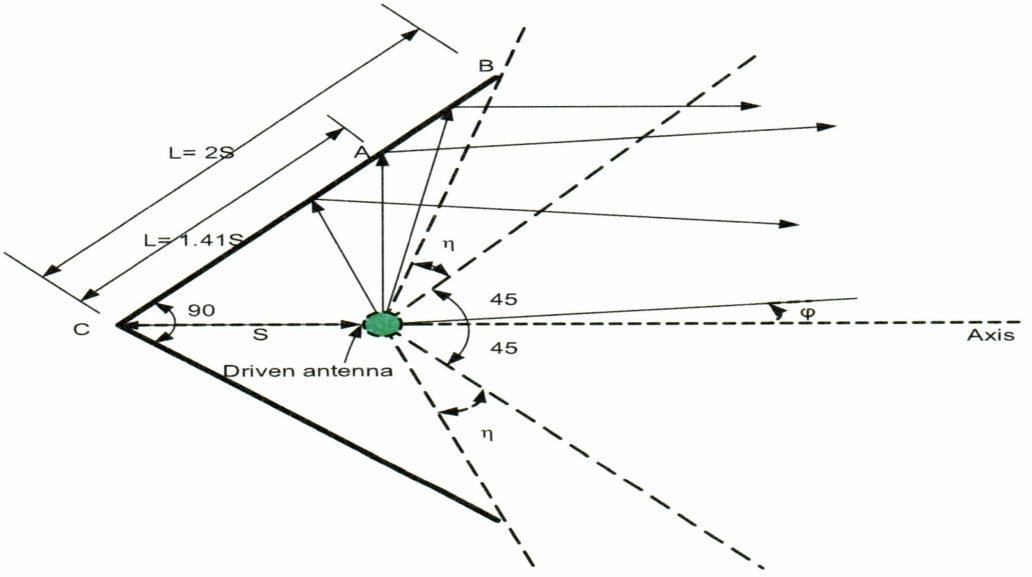

Figure 2.13 Square Corner Reflecting Antenna Analyzed Using Ray Tracing [10].

The design in our project follows the design guidelines for a 90° corner reflector with bow-tie dipole for wide band provided in Table 2.2, but optimized using a NEC software package called NECWINPRO, to get a feasible size. Figure 2.14 depicts the construction model of corner reflector antenna, which also elucidates terms used in Table 2.2. Figure 2.14 displays the number of wires used in building the reflector and feed elements, the lengths of which are mentioned in Table 2.3. In Figure 2.14, R represents the reflector wire length, S is the source to corner spacing, l is the square biconical dipole length, d is the reflector wire diameter, s is the reflector wire spacing, and L is the reflector length.

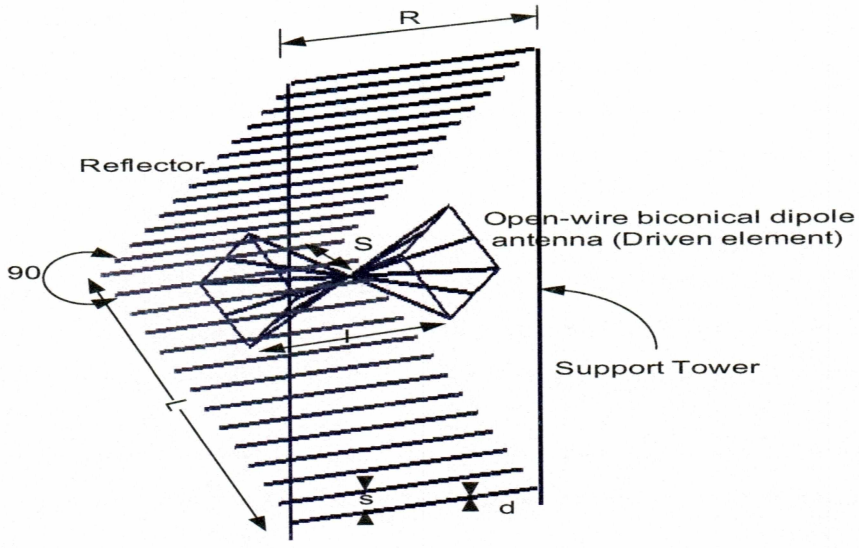

Figure 2.14 Square Corner Reflector Antenna with Biconical Dipole for Wideband Operation.

None of the corner reflector dimensions mentioned in Table 2.2 is critical. A moderate change in values of L and R might result in small changes in gain. The dimension R is generally chosen from 1.2 to 1.5 times the length of the feed, so as to minimize the back region radiation.

Table 2.2 Design Data for Wideband 90^0 Corner Reflector with Bow-Tie Dipole [10].

	Lowest Frequency f1	Mid Frequency f2	Highest Frequency f3	Units
S	0.27	0.40	0.54	λ
L	0.75	1.13	1.50	λ
R	0.81	1.20	1.62	λ
s	0.061	0.092	0.122	λ
D	0.01	0.015	0.02	λ
l	0.53	0.80	1.06	λ
Gain	11	13	14	dBi

The actual antenna dimensions over a 2 to 1 frequency range (9 to 18 MHz) are listed in Table 2.3. It was observed that though there was significant change in dimensions used, the gain was not much affected. The antenna dimensions in meters are presented in Table 2.4.

Table 2.3 Design Data for Wideband 90^0 Corner Reflector with Open Wire Biconical Dipole.

	Lowest Frequency f1 9 MHz	Mid Frequency f2 13.5 MHz	Highest Frequency f3 18 MHz	Units
S	0.258	0.387	0.516	λ
L	0.56	0.83	1.10	λ
R	0.48	0.72	0.96	λ
s	0.03	0.045	0.06	λ
d	7.76×10^{-5}	1.16×10^{-4}	1.55×10^{-4}	λ
l	0.396	0.594	0.792	λ
Gain	9.8	12.23	13.25	dBi

Table 2.4 Design Data Represented Using Different Units.

	Lowest Frequency f1 9 MHz	Mid Frequency f2 13.5 MHz	Highest Frequency f3 18 MHz	Units
S	8.600	8.600	8.600	meters
L	18.667	18.444	18.333	meters
R	16.000	16.000	16.000	meters
s	0.999	0.999	1.000	meters
d	2.586×10^{-3}	2.577×10^{-3}	2.583×10^{-3}	meters
l	13.200	13.200	13.200	meters
Gain	9.8	12.23	13.25	dBi

Modeling the radiating structure in NECWINPRO yields the azimuthal radiation pattern shown in Figure 2.15.

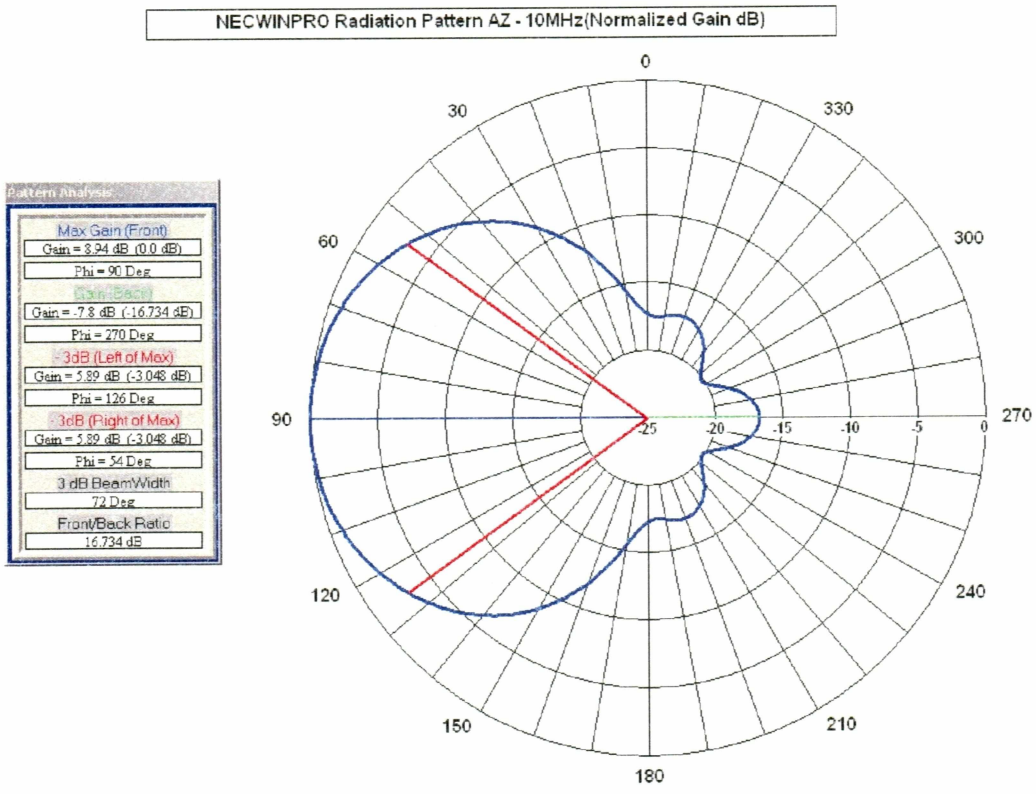

Figure 2.15 NECWINPRO Radiation Pattern 10 MHz-AZ.

The gain of the antenna at the shown frequency of 10 MHz is 8.94 dBi. The front-to-back ratio and 3 dB beam widths are 16.734 dB and 72°, respectively. Similarly, the elevation radiation pattern for the antenna is shown in Figure 2.16.

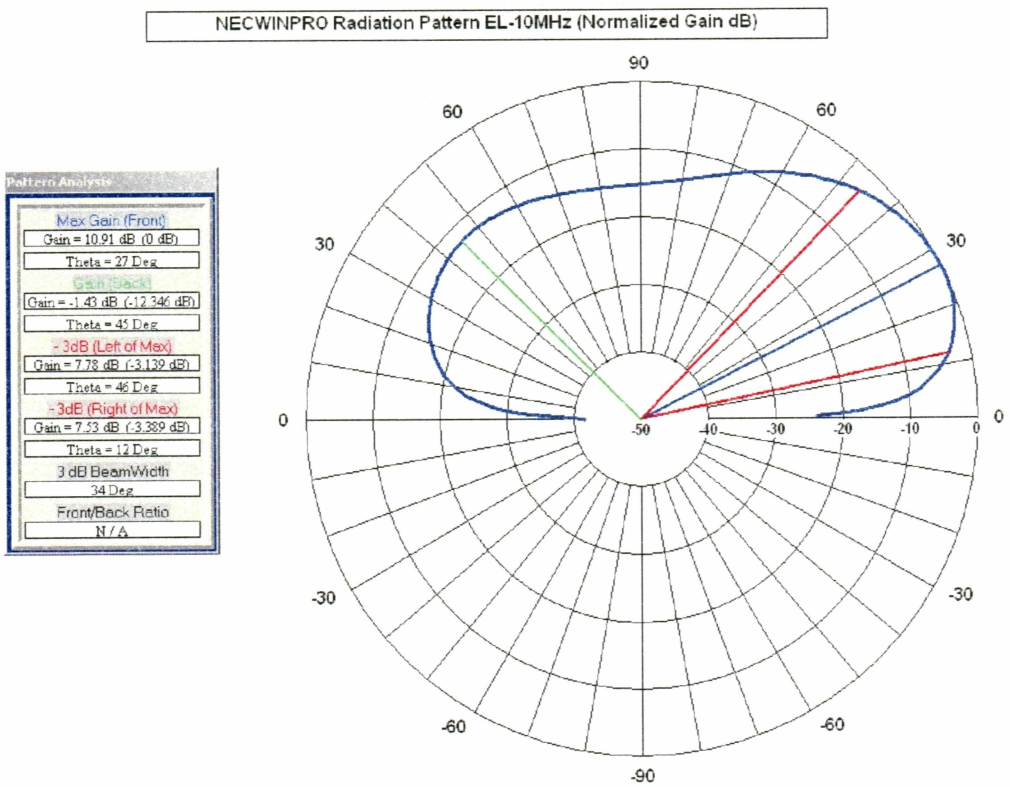

Figure 2.16 NECWINPRO Radiation Pattern 10 MHz-EL.

The gain of the antenna at the shown frequency of 10 MHz is 10.91 dBi. Here, the peak of the main lobe is at 27° above the horizon, with a 3 dB beam width of 34°. A plot of VSWR over the band of operating frequencies is shown in Figure 2.17. Looking at the plot, one can make out that, except at lower frequencies, the antenna's performance is fairly acceptable through out the band.

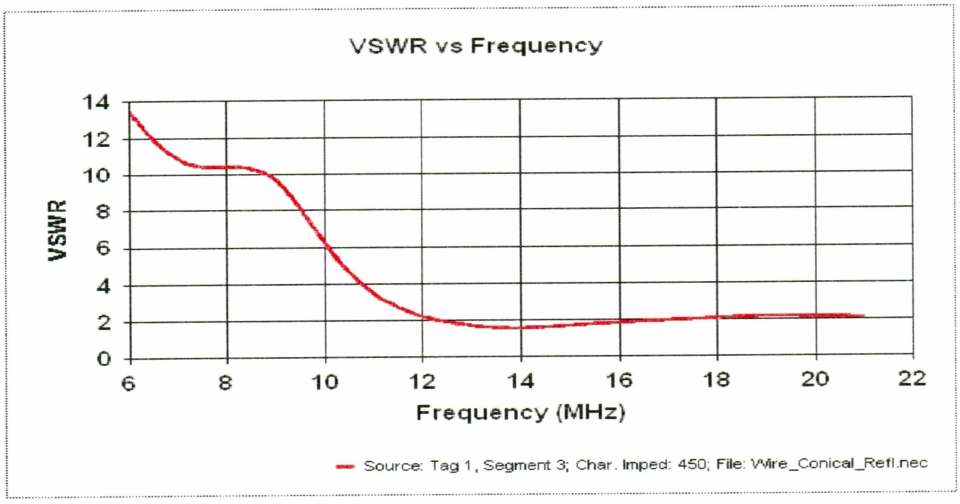

Figure 2.17 VSWR vs Frequency Plot of Square Biconical Corner Reflector.

2.4 GPS Clock Card

The model 560-5908 (GPS-PCI 2) clock card was manufactured by Truetime, which is now part of Symmetricom. This card has been used to obtain precision timing in my project. The 560-5908 receives the transmissions from the NAVigation Satellite Timing And Ranging (NAVSTAR) GPS satellite system and derives time that is traceable to the National Institute of Standards and Technology (NIST) [12].

2.4.1 Clock Card Specifications

The model 560-5908 (GPS-PCI 2) clock card, which shall be referred to as the clock card hereafter, is a single-slot peripheral component interconnect (PCI) compatible short card, 6.85" long. It is specified to have a timing accuracy of < 1μs. It uses coarse acquisition code, tracking 8 satellites at a time. The clock card can be used in two modes, either as a generator or synchronized generator. In synchronized generator mode, it is synchronized by an external reference. The on-board oscillator is disciplined to this input reference so that card's drift rate is a function of the external reference, thus supplying precise time (hundreds of nanoseconds

through thousands of years) to the host computer. The GPS is one of the input references that could be used as a synchronizing source [12]. In order to get microsecond accuracy in time difference measurement, and to achieve a reliable synchronization between transmit and receive ends, the clock cards were configured to operate in synchronized generator mode with GPS being the input reference signal. For GPS synchronized generator mode, the unit requires an external antenna. There is a standard antenna supplied with the card. The general specifications of antenna and cable are shown in Table 2.5.

Table 2.5 Antenna and Cable Specifications [12].

Specifications	Antenna	Cable
Weight	0.55 lb	
Operating temperatures	-40° C to 70° C	-40° C to 70° C
Power	25 mA @ 12 V	
Type		RG-59
Connectors		TNC male to BNC

No functional block diagrams were provided by the manufacturer despite my requests. Hence, the following discusses the functionalities of different register sets and gives a brief overview of their functioning.

Data registers on the PCI card are mapped into the PCI memory space and are used to control, configure, and report information on the PCI card. All the locations are described as an offset from the PCI base address register-2 (3rd address). The PCI card uses PLX 9050 interface chip. It has a block of 32 double word registers reserved for local configuration purposes. These local configuration registers are physically mapped to both memory and to I/O address space at runtime.

2.4.2 *Overview of PCI Card Control /Status Registers*

The configuration registers control the configuration of the PCI card. They are used to select the mode of operation, to preset the GPS position, and to set the event active edge. The diagnostic register contains the results of internal diagnostic tests performed at power up and during normal operation.

The event time capture registers are used to capture the time of an event. The event may be selected to be an external event or one of the following PCI card generated signals, a rate generator, a rate synthesizer, or time compare. The hardware control and hardware status registers handle the PCI card interrupt sources and the status flags for the event, time compare, rate generator, rate synthesizer, and antenna open/short.

The signal level registers contain the satellite numbers and signal levels of up to six satellites when in the GPS synchronized mode. The software time capture and antenna position freeze registers are updated by writing to the low order freeze register. The time registers contain thousands of years through hundreds of nanoseconds [12]. The position registers used only in the GPS synchronized mode, contain GPS position latitude, longitude and elevation.

2.4.3 *The Synchronized Generator – GPS Mode Outline*

The synchronized generator mode steers and phase locks the on-board oscillator to the timing provided by a GPS receiver. The PCI card time is automatically set by the time provided by the GPS receiver. If the GPS receiver indicates that a good time is available, the card transfers GPS time into the generator time registers. When the PCI card is within the timing specifications, the "locked GPS" flag is set in the time register. With the satellites visible, the card will normally lock within 10 minutes.

Time and status are available via the PCI bus in the three, 32 bit words. Each word contains packed binary coded decimal (BCD) time values. This time can be captured either by writing to an address that latches the time in a set of registers or an event (selectable to be external) signal can latch the time in a second independent set of registers, permitting time

tagging of an event. An event can generate an interrupt to flag its occurrence and the time can then be read over the bus. A brief discussion of both the methods follows [12].

2.4.4 Software Time Capture

This feature provides the PCI card's time at the time of request. Writing to the software time capture register freezes the current time of day in the software time registers, which contain packed BCD data, and a status bit. The PCI card will capture the software time request at the time of arrival, but there is 40 to 400 μs delay after the time request before the time is available in the time registers. The PCI card has a software time ready bit in the hardware status register location that may be used for handshake control. Prior to reading the satellite data, the satellite update status should be checked and data should be read only when the location is zero. If the software time request occurs too fast (< 400 μs apart), the time may not be stable in the registers, and read errors may occur [12].

Procedure:

- Freeze the time by writing any value to the software time capture register.
- Wait for the software time ready bit. When the bit is set, read the time.

2.4.5 Event Time Capture

This feature provides the PCI card's time at the time of an event. The PCI card will capture the event at the time of the arrival. The PCI card has from 40 to 400 μs delay after the event before the time is available in the time registers. The PCI card has an event bit in the hardware status register that may be used for handshake control. Prior to reading the satellite data, the satellite update status should be checked and data should be read only when the location is zero. If the event time request occurs too frequently (< 400 μs apart), the time may not be stable in the registers, and read errors may occur [12].

Procedure:

- Set the event time capture control register for the desired event source. The event may be selected to be external, rate generator, rate synthesizer or time compare.
- Set the triggering edge (rising edge or falling edge) using the event trigger edge control register.
- Wait for the event bit. Read location, when the bit is set, read the time.

2.5 Receiver Card

Echotek's model GC214-PCI/TS, digital receiver card is used as the receiver board in this project.

2.5.1 Specifications

The Echotek model GC214-PCI/TS, digital receiver card, which shall be referred to as GC214 hereafter, is a four channel receiver board designed to support wireless communication applications. ECDR-GC214-PCI/TS can accept two IF/RF analog inputs. It digitizes them using 14 bit-A/D converters, and then down converts and filters the digitized data for either input. These data are resampled to adjust the output sample rate and processed data are stored in a sample FIFO memory. These data can be read from FIFO memory over the PCI bus or can be transferred to PCI memory using DMA controllers [13].

The sustained data rate of moving samples out from the PCI interface depends on several factors, like burst data rate with DMA controller overhead, crossbar delays, bridge chip delays and bus traffic. On a good dedicated system like the one which we use in our project, the data throughput rate is between 90 to 120 MB/s. This speed is essential as we deal with limited FIFO size at high output rates.

The PCI interface is implemented through a PLX PCI9080 interface chip, which provides two direct memory access controllers. There is no local memory for linked-list

storage as there is no random access memory (RAM) on the GC214. All control registers including FIFO memory are mapped into PCI memory space.

There are two DMA channels in GC214 and two DMA transfer complete interrupt bits on PLX PCI9080 which are controlled by PCI9080 registers. Before accessing the GC214, several local registers in the PCI interface and DMA controllers (DMACs) must be configured for data collection. The GC214 stores receiver samples using a FIFO buffer, which extends up to 128K x 32 for each receiver channel, accounting for about 512K x 32 overall FIFO memory space.

A functional block diagram of GC214 is shown in Figure 2.18, which shows the four receiver channels that are available. Any of these four receiver channels can be configured through software to select either one of two RF/IF inputs.

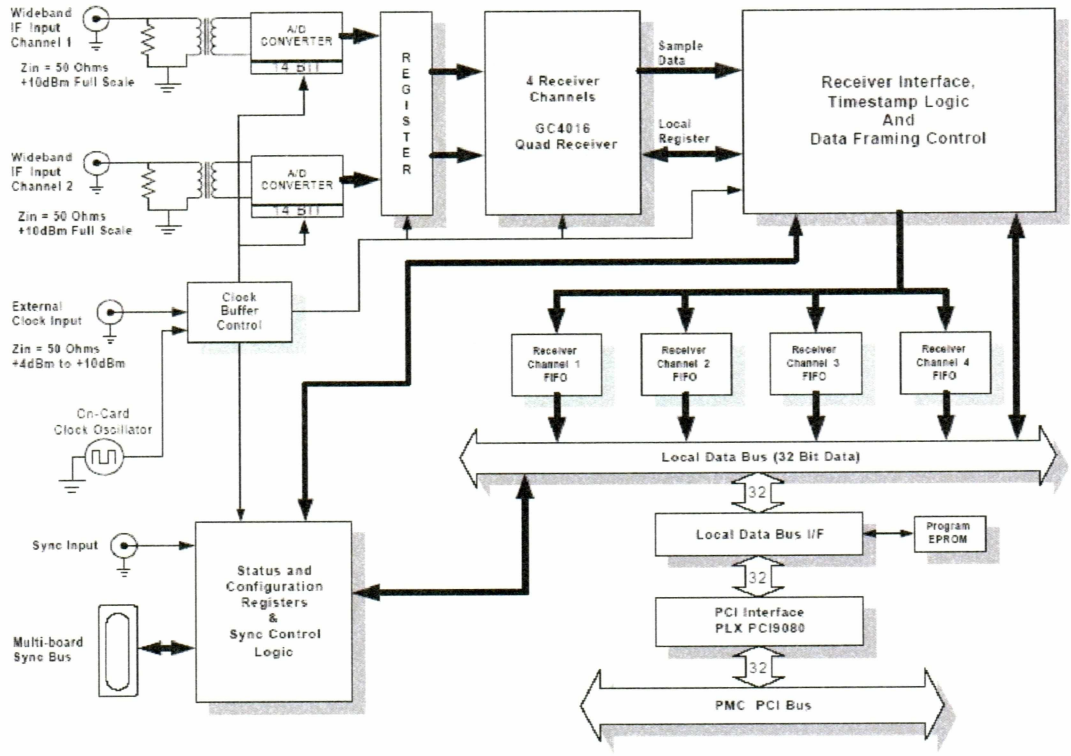

Figure 2.18 Functional Block Diagram of GC214 [13].

As shown in the block diagram, these inputs are transformer coupled into A/D converters, which separate DC. Typical 1 dB input bandwidth of the coupler ranges from 150 kHz to 200 MHz.

Analog Devices AD6644AST-65 chips are used as A/D converters in this card, which are claimed to operate at a guaranteed minimum of 65 MHz. They are 14 Bit A/D converters and designed to provide greater than 90 dB of spurious free dynamic range (SFDR). Each one of four independent receiver channels consists of a GC4016 channel, data formatting and framing logic, and a FIFO as shown in Figure 2.19.

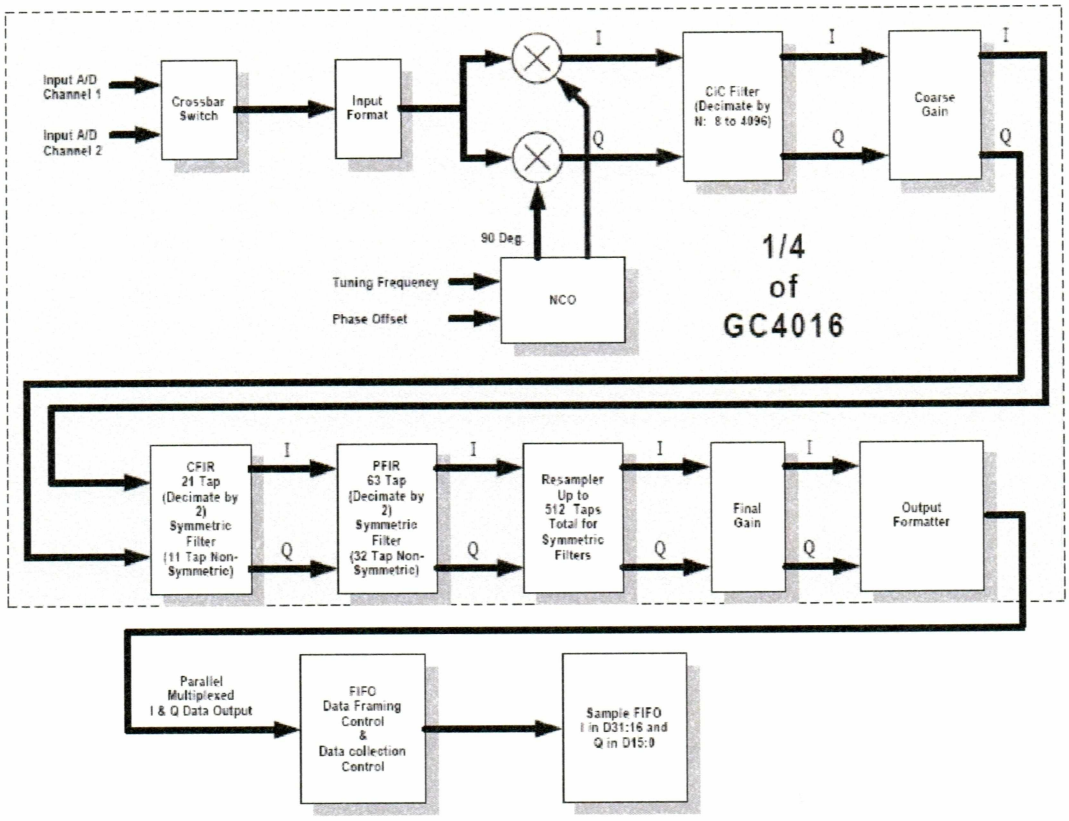

Figure 2.19 Functional Diagram of Each Receiver Channel [14].

As shown in Figure 2.19, each receiver channel includes a five stage cascaded coherent integrator comb (CIC) filter, which reduces sample rate by a programmable decimation factor ranging from 8 to 4096 [14]. These outputs are followed by a coarse gain stage. This stage boosts the gain of weak signals up to 42 dB in 6 dB steps, and this stage is followed by two stage filtering. A 21 tap symmetrical coarse finite impulse response (CFIR) low pass filter is the first among two stages of filtering, and decimates signal by a factor of two. The second stage is a 63 tap precision finite impulse response (PFIR) filter. This further decimates the signal by another factor of two. Both these filters were programmed as there were no default filter coefficient sets. The numerically controlled oscillator (NCO), or mixer circuit, tunes the center frequency to the base band, from which it could be low pass filtered by the CIC, CFIR, PFIR and resampler.

Four receiver channels could be configured as four narrow band channels, two wide band channels, or one extra wide band channel, depending on the requirements of the application. The following Table 2.6 gives the decimation ranges, bandwidths, and FIFO sizes for each configuration. We configured the card into four narrow band channels to meet our requirements, which will be discussed in detail in the forthcoming chapters.

Table 2.6 Receiver Channel Combinations [13].

Receiver Channels	Maximum Bandwidth*	Minimum Bandwidth*	Decimation Range	FIFO Size
4 narrowband	2.1875 MHz	2.135 kHz	32 to 32768	Channels 1 through 4
2 wideband	4.375 MHz	4.27 kHz	16 to 16384	Channels 1 and 2 only
1 extra-wide band	8.75 MHz	8.54 kHz	8 to 8192, (16 to 8192 in 20-bit data mode)	Channel 1 only

Chapter 3. The System Design and Implementation

This chapter explains the design implementation of the system that calculates the virtual reflection height of the ionosphere. The chapter starts with a brief description of the overall design strategy and the design specifications. The various steps that were followed to configure the equipment used in the design and various problems that were faced during the process are presented. The signal processing and analysis are discussed at the end of the chapter.

The equipment used in the design, as explained earlier, includes a receiver antenna, a receiver board to receive and process signals at different frequencies, a time synchronizing source, and a dedicated computer. The receiver antenna constructed at PFRR is an open wire biconical dipole corner reflector, which has been described in Chapter 2. A brief description of the GC214 receiver board used in this project has been given earlier. The GPS timing was used as synchronizing source. A brief description of Truetime's model 5908 clock card has been mentioned in previous chapter. The following topics explain the steps followed in configuring the hardware to accomplish the aforementioned tasks.

The overall strategy in brief is that the GC214's four channels must be dedicated to the first four lowest frequencies mentioned in Table 2.1. Then the GC214's data collection should be synchronized to GPS time using the clock card. As both the GC214 and the clock card could be synchronized by an external trigger, the parallel port of the computer system is chosen to be the external synchronizing source. The moment the parallel port supplies an external trigger, the clock card records the GPS time and the GC214 starts collecting samples at four different frequencies. The incoming samples are stored in a RAM-disk and processed. Once the processing is done and the sample number of the received pulse's rising edge is determined, then the sample number is multiplied by the sample period and added to the base time provided by the clock card, which gives the time of transmission of the pulse. This process is depicted in Figure 3.1.

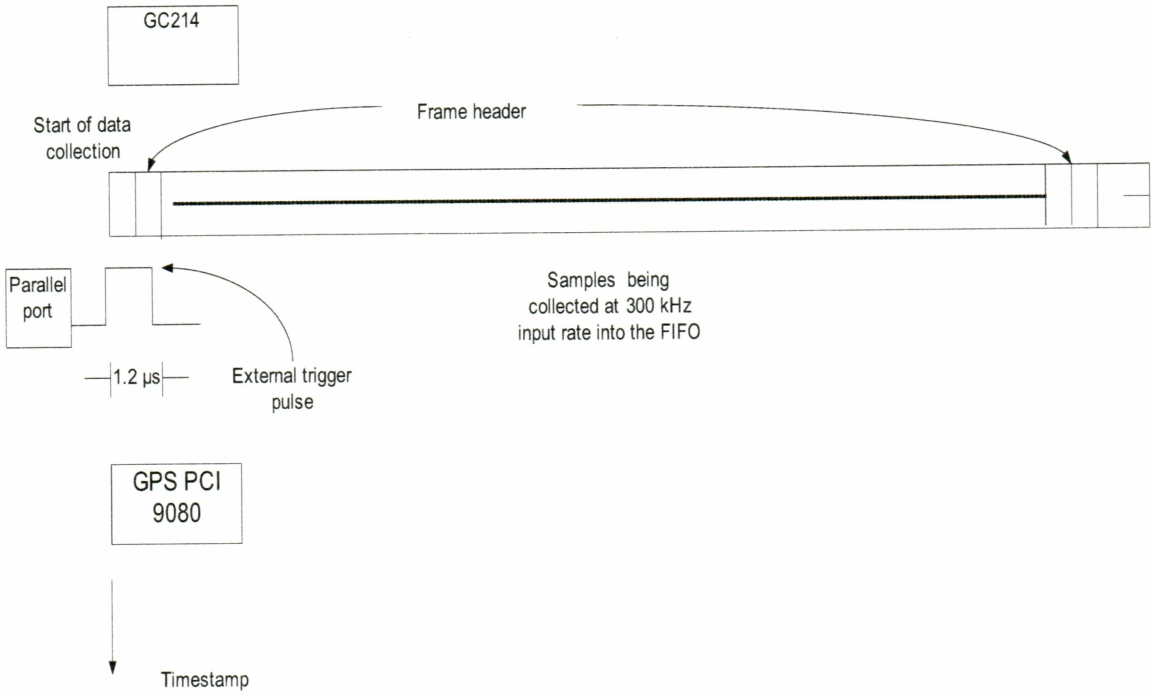

Figure 3.1 The Overall Strategy.

3.1 Specifications

The Kodiak SuperDARN radar operates in the 8 to 20 MHz frequency band scanning a 52° azimuth sector. There are 16 narrowly spaced beams, each ~3.25° apart. Typically, the radar performs 1 or 2 min scans using 3 or 6 s integration time per beam, depending on the mode of operation. These azimuth scans begin on whole minute boundaries, which typically lead to ~12 s down time where in no useful data are collected. To utilize this down time a new mode of operation, called sounding mode, was developed. In this mode the radar steps through the group of fixed frequencies mentioned in Table 2.1, with a 1 s integration period on each beam. The complete 52° azimuth scan at each frequency in sounding mode is possible only

after a considerable number of normal azimuth scans and it might take roughly 10 to 15 minutes.

This project was aimed at designing a receiver that would observe transmissions of the sounding mode on the ground at a point in the field of view of the radar. By measuring the time of flight of transmissions from the radar to the ground point, the ionospheric reflection height can be estimated.

In our design we use the Kodiak SuperDARN radar network as the transmitter. An optimum site to place receiver should not only fall within the coverage range of the Kodiak radar field of view, but also lie beyond the skip distance for average conditions. Considering the above mentioned requirements, two potential sites were selected, Inuvik and Toolik lake, shown in Figure 3.2. Both these sites are under the field of view of radar at ranges that would often lie beyond the skip distance for the frequencies used in the sounding mode.

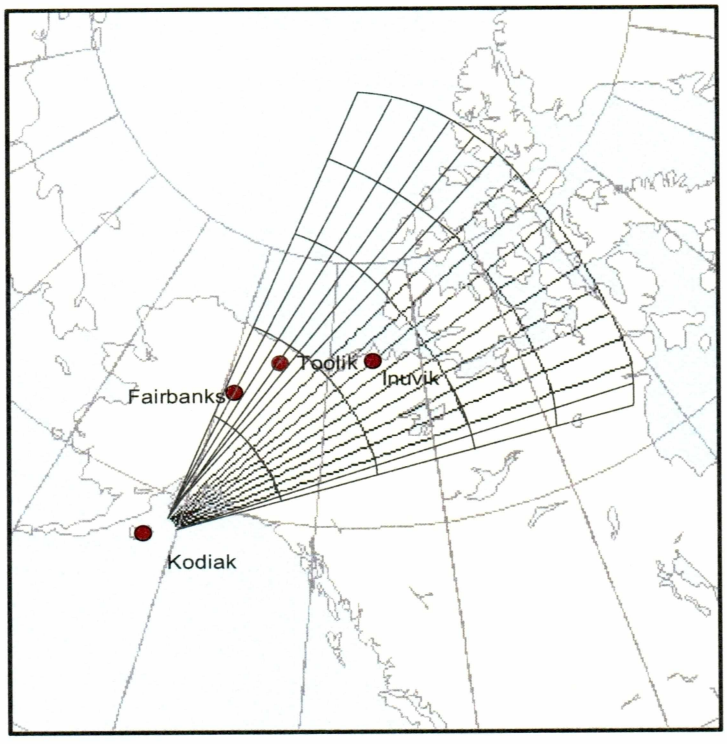

Figure 3.2 The Best Available Locations for the Receiver Antenna Construction.

However, due to some practical problems we ended up constructing antenna at PFRR, which falls within the skip distance range for most of the higher frequencies used in sounding mode. But for the low frequencies used, the range is optimum. Further, building the system close to Fairbanks had the benefit of easy access for debugging.

Hence, the task was redefined to look at the four lowest frequencies in the sounding mode, and detect the time of occurrence of the pulse transmitted by Kodiak SuperDARN. In short, the receiving module consisting of the antenna and the GC214 collects and processes samples. Two clock cards, one each at the transmitter end and the receiver end, register the transmit time and arrival time of pulses. The difference in times gives the time of flight of the pulse, from which we calculate the virtual reflection height, assuming the pulse travels with the velocity of light (3×10^8 m/s), all through its flight.

3.1.1 The Pulse Sequence

The radar at Kodiak transmits a unique pulse sequence, as shown in Figure 3.3, which contains 7 pulses, each with duration of 300 μs. The 7 pulses in a pulse sequence are each transmitted at 0T, 9T, 12T, 20T, 22T, 26T and 27T, respectively, where T = 2.4 ms is the fundamental pulse separation period. The total time to transmit a pulse sequence is ~65 ms. There is a ~100 ms separation between the start of one pulse sequence and the start of the subsequent sequence. This corresponds to ~70 pulses every second. The autocorrelation function of the echo signal received from this pulse sequence is used to derive valuable information regarding targets, like Doppler frequency, power, and spectral width. Though my project is not intended to calculate Doppler frequency, with a slight modification in code this could be achieved, which might be considered for future work. The uniqueness of the transmitted pulse sequence makes detection easier at the receiver end.

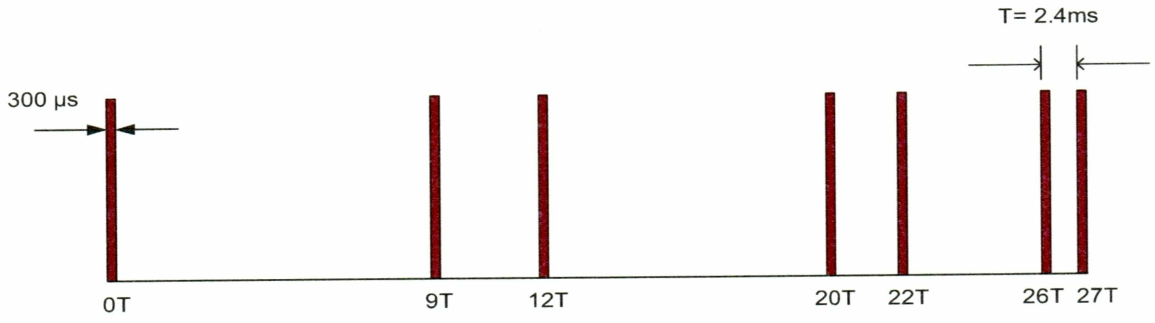

Figure 3.3 Pulse Sequence Model Generated by Kodiak SuperDARN.

3.1.2 The QNX Operating System

The first thing to consider after selecting the hardware is to develop application oriented software. The operating system used by all the SuperDARN community is QNX, which is a multi-tasking and multi-user, real-time operating system.

QNX has some important characteristics like pre-emptive scheduling, inter-process communication mechanisms, minimal interrupt latencies, fast context switching, and simple semantic kernel functions with quick execution times, which make QNX an optimum operating system for real-time operations [15]. Hence this operating system and the generic versatile high level programming language C were chosen as building tools for my software development. There were no drivers available for the clock card under QNX. Hence, software had to be written from scratch. For the GC214, the driver developed by another student, Todd Parris, was used as a reference, and a new code was developed to suit my task.

3.2 Configuring the Clock Card

The critical issue in this project is timing, and both the transmitter and the receiver must be time synchronized. The time of transmission and reception of a pulse should be determined accurately. As mentioned, the Truetime's model 5908 clock card was used in

synchronized generator mode, which when programmed locks itself to GPS satellites and supplies microsecond level accurate timing.

The radar gets its timing from a dedicated computer system used for timing and control, which initiates an integration based upon the time from the computer's system clock. Every computer has its own built-in clock, which keeps track of the date and time even when the machine is turned off. These built-in clocks often drift by a second or two in the course of day. Most applications do not need this degree of accuracy, so usually users neglect this drift. The operating system itself will try to compensate for the drift due to known problems with round off errors, etc. Because our application is time critical, the drift is not considered acceptable, and an algorithm has been developed to set the system time to GPS reference time once in every ten seconds if there is any drift. The following pseudo-code (Figure 3.4) explains the process and QNX core functions used in this process. This code utilizes the software time capture procedure explained in Chapter 1.

MAIN

Initialize the PCI configuration registers

Set system resolution

INFINITE LOOP

Check board and antenna conditions

Wait for GPS lock

If lock is attained, then

Read system time "clock_gettime"

Freeze GPS time

Sleep for 499 μs

Read GPS time

Add to seconds and nanoseconds from 1970

Add 499 μs to nanoseconds and set system time "clock_settime"

```
Measure difference in system time and GPS time
        If difference is less than 500 ns, break
                Set the hardware clock to GPS using "rtc" (once in 24 hours)
        Else
                Go to: Beginning of loop.
Sleep ten seconds
Go to: Beginning of loop.
```

Figure 3.4 Pseudo-Code Illustrating the Procedure Followed to Synchronize the System Time to GPS Time.

In general, when we call the "clock_gettime" function, we retrieve a structure that contains time in seconds since 1970 and number of nanoseconds elapsed in the current second as the system clock is a data structure containing the current time. Here it should be noticed that the system clock does not increase in one nanosecond increments. It increments in multiples of clock's resolution, which is typically 10 ms depending on CPU speed [15]. This posed problems in adjusting the computer time to GPS time. Hence, using the "clock_setres" function, the computer time increment resolution was adjusted to 499 μs, which is the maximum attainable resolution in the QNX4 operating system.

Once the system resolution is set, the system time is read using "clock_gettime" function and is set to GPS reference time following the procedure in pseudo-code. As the code starts, the PCI configuration registers are initialized and system resolution is set. Then code enters an infinite loop where in it checks for the board and the antenna conditions by reading the diagnostics and hardware status registers briefed in Chapter 1. If they are diagnosed to be ok, the code waits until it locks to GPS. When lock is attained, the system time is read using "clock_gettime" function. At this moment, the GPS time is frozen as explained in software time capture procedure in Chapter 2. Then, the GPS time is read and stored in a buffer. In order to use memory effectively, the standard format of storing time in seconds and

nanoseconds since 1970 has been followed. So the code reads current seconds and nanoseconds from a clock card and adds them to the seconds and nanoseconds since 1970. The seconds and nanoseconds are stored as two separate unsigned long integers. Now the lag of 499 μs is added to the system time and the difference between the system time and the GPS time read from the clock card is measured. If this difference happens to be less than 500 ns, the code quits the loop, if not it repeats the above procedure until that accuracy is attained. This is how the system time is adjusted to GPS time. Also, to account for occasional reboots once a day, the hardware clock is set using "rtc –s hw" command. This resets the hardware clock to current system time, which has been adjusted to GPS time using above mentioned procedure.

Timestamps of pulses transmitted by the radar are registered at the moment they are being transmitted and received to calculate time of flight. I use the rising edge of the pulse being transmitted as an external trigger to the GPS card, and register the time stamp of each pulse being transmitted at the transmit end. The following pseudo code explains the procedure involved in getting the timestamp of an external trigger.

MAIN

Initialize the PCI configuration registers

Set system resolution

INFINITE LOOP

Check board and antenna conditions

Wait for GPS lock

If lock is attained, then

Wait for external event bit

If external event occurs

Read EVENT time

Add to seconds and nanoseconds from 1970

Open file name with "current hour" embedded in filename

Write time stamp to the file

Go to: Beginning of loop.

Figure 3.5 Pseudo-Code Illustrating the Procedure Involved in Getting the Timestamp of an External Trigger.

As the code starts, the PCI configuration registers are initialized. Then the system resolution is set and the code enters an infinite loop where in, it checks for the board and the antenna conditions by reading the diagnosis and hardware status registers. If they are diagnosed to be ok, the code waits until it gets a GPS lock. When the lock is attained, code waits for the rising edge of the transmit pulse to set an external event bit. At that moment the event time is read utilizing the event time capture procedure and is stored in a buffer. The code reads current seconds and nanoseconds from the card and adds them to seconds and nanoseconds since 1970. In addition, code opens up a new file every hour and registers the time of occurrence of every single pulse sequence transmitted by the radar.

3.3 Configuring the GC214

The receiver functions include sampling the RF signal, mixing the RF signal to baseband, decimating the signal, filtering the signal, formatting the output and providing the filtered baseband samples, which are later used by the signal processing code [9].

3.3.1 Sampling

As shown in Figure 2.18, the two RF/IF inputs on the GC214 digital receiver are digitized by an Analog Devices model AD6644AST-65 analog-to-digital converters. The ADC6644AST-65 is a 14-bit ADC that is triggered by the external clock input on the GC214 provided by the 65 MHz reference signal. The output of each of the ADCs can be routed to the input of any of the four GC4016 digital receiver channels on the GC214 digital receiver [13].

As mentioned in Chapter 2, the GC214 was configured to have four narrow band channels, each being dedicated to receive data at a particular frequency such that the four lowest frequencies in the sounding mode table (Table 2.1) are accommodated. Since PFRR falls within skip distance for most of the high frequencies, they were neglected in the current project.

3.3.2 Mixing

The first stage in each of the receiver channels is a digital mixer. The sampled RF signals from the ADCs are mixed with signals from an NCO. There is one NCO in each of the four receiver channels. The frequency of each NCO is programmed by a 32 bit register that defines a clock division factor [9]. The tuning frequency is set to the FREQ register according to the formula $FREQ = 2^{32} F/F_{ck}$, where F is the desired tuning frequency and F_{ck} is the chip's clock rate (65 MHz). The 16 bit phase offset is $PHASE = 2^{16}P/2\pi$, where P is the desired phase in radians ranging from 0 to 2π.

3.3.3 Decimation

As mentioned earlier, the radar performs a clear frequency search in sounding mode within a bandwidth of 200 to 250 kHz from the center frequency. To obtain the center frequency, the sounding mode code considers frequencies mentioned in Table 2.1 as the lower bounds in a frequency band and adds 300 kHz to them to get the upper bounds. The code then takes the arithmetic mean of the lower and upper bounds to obtain the center frequency. Within a bandwidth of 200 to 250 kHz from the center frequency the radar searches for a clear frequency and transmits the signals in that frequency. Since the exact frequency of transmission is not known by the receiver, the receiver is tuned to receive a bandwidth of 300 kHz from the defined center frequency. As we are looking at 300 kHz bandwidth, the output rate needs to be at least 300 kHz in order to satisfy the Nyquist criteria of signal reconstruction, and overall decimation is used to set the output data rate.

After the mixing stage in each of the four receiver channels, there is a CIC decimator. The CIC has several control registers associated with it. One of these registers sets the

decimation factor. It should be noted that there are two stages of finite impulse response filtering after the CIC. Each of these stages of filtering decimates the signal by a factor of two, so the decimation factor of the CIC is set to be one-fourth of the total decimation value required. As the RF signal is sampled at 65 MHz, attaining an output sample rate of 300 kHz requires an overall decimation factor of 216 (65 MHz/300 kHz = 216), which results in the CIC decimation of 54.

There is an algorithm in the new digital receiver driver that reads the desired filter bandwidth and sets the decimation of the CIC accordingly, such that the output rate is equal to filter bandwidth. But for my application the filter bandwidth is fixed and hence the decimation.

3.3.4 Filtering

Two stages of filtering follow the CIC decimator in each of the receiver channels. The first is a 21 tap FIR filter, which provides coarse filtering; hence the name CFIR. The second stage of filtering is a 63 tap filter which provides more precise filtering and hence is called PFIR. These two filters in combination provide all of the base band filtering [9].

The filter coefficients for both of these filters are determined by first defining the ideal frequency response of the filters in the frequency domain. The frequency response of an ideal discrete lowpass filter, $H_{LP}(e^{jw})$, is simply a step function defined by

$$H_{LP}\left(e^{j\omega}\right)=\begin{cases}1, & |\omega| \le \omega_c, \\ 0, & \omega_c < \omega \le \pi,\end{cases} \qquad (33)$$

where ω is the frequency in radians, and ω_c is the desired cut-off frequency, and 2π is the sample frequency [16]. The impulse response coefficients, $h_{LP}[n]$, of this ideal filter are

$$h_{LP}[n]=\frac{\sin(\omega_c n)}{\pi n}, \qquad -\infty \le n \le \infty. \qquad (34)$$

Since there are only 21 coefficients in the CFIR filter and 63 in the PFIR filter, the infinite impulse response cannot be realized. A truncated impulse response must be used, which introduces the oscillatory behavior of Gibbs phenomenon [16]. To minimize the effects of Gibbs phenomenon, the truncated filter coefficients are multiplied by a Hamming window. Also, to provide linear phase through the filter, symmetric filter coefficient filters are used. The filter coefficients of the both the CFIR and PFIR filters for 300 kHz bandwidth are shown in Figure 3.6.

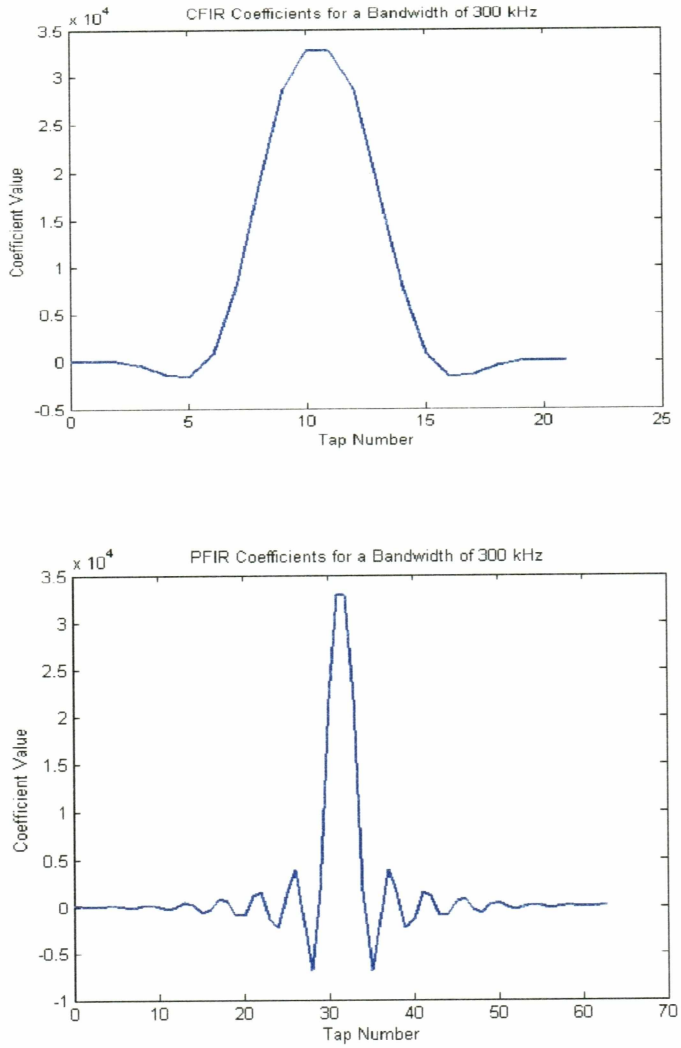

Figure 3.6 CFIR and PFIR Filter Coefficients for a Filter Bandwidth of 300 kHz.

It should be noted that, since the CFIR filter decimates by a factor of two, the sample rate into the PFIR filter is half of the sample rate into the CFIR filter. Since the sample rate into the CFIR is twice the sample rate into the PFIR, and the CFIR has fewer filter coefficients, the frequency response of the CFIR for narrow bandwidths is less than ideal. When the two filters are used together, however, a good frequency response with good out-of-band rejection can be achieved. The frequency responses of both the CFIR filter and the PFIR filter are provided in Figure 3.7.

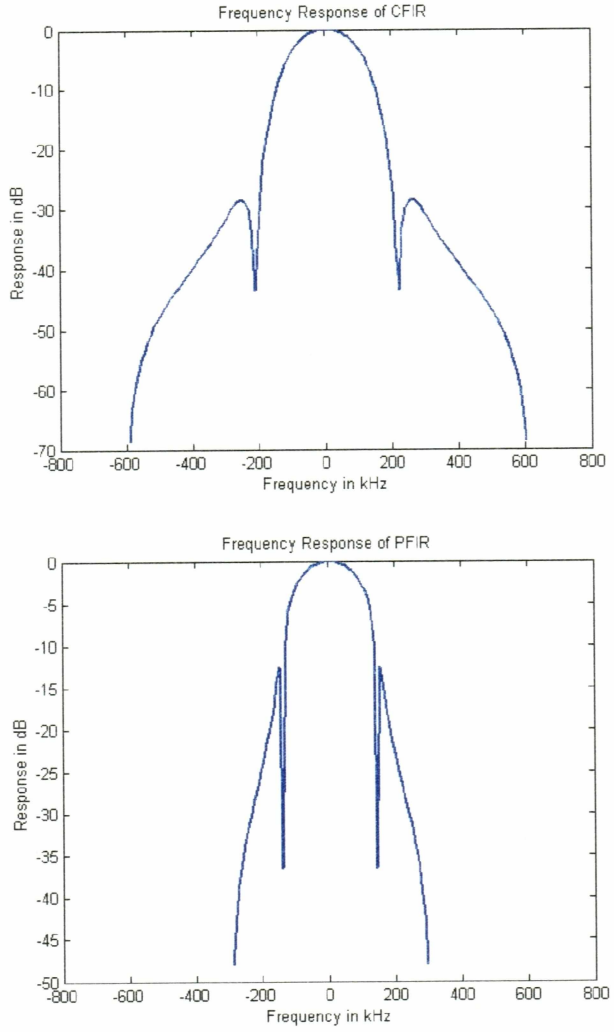

Figure 3.7 Frequency Responses of the CFIR and PFIR Filters for a Bandwidth of 300 kHz.

Since the CFIR filter and PFIR filter are cascaded, the frequency response of the two filters in series acts on the baseband signal in the digital receiver. The frequency response of the two filters in series is provided in Figure 3.8.

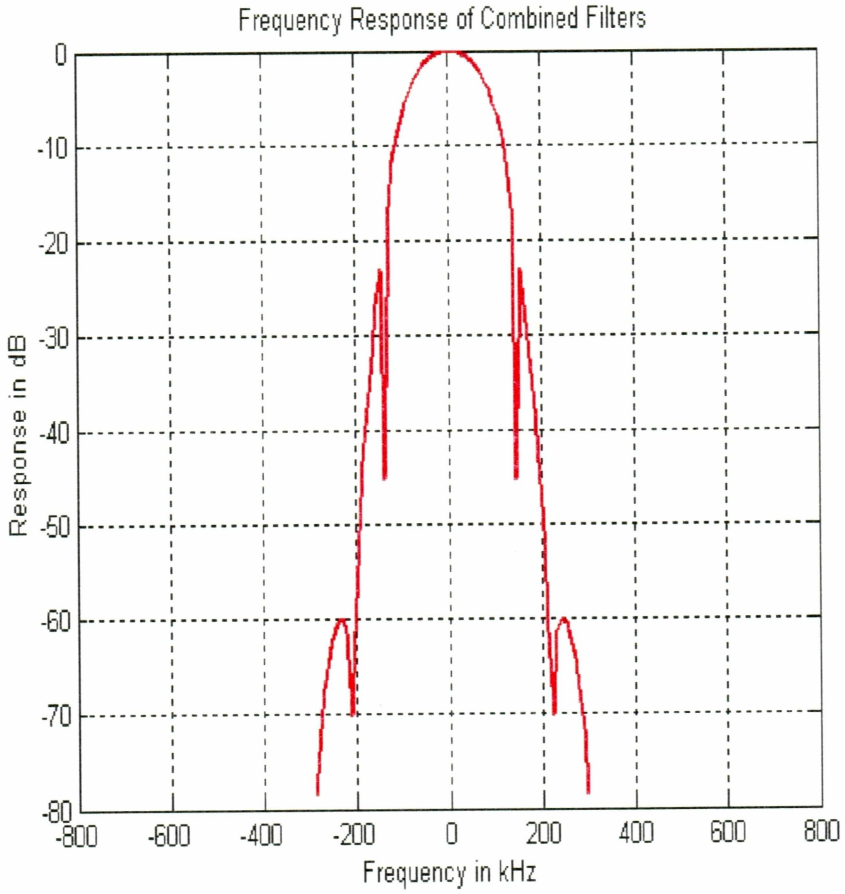

Figure 3.8 Total Frequency Response of the Filtering Stages on the Digital Receiver for a Bandwidth of 300 kHz.

The final filter has a 6 dB bandwidth of 225 kHz, and the frequency response drops to less than -65 dB in an octave and less than -75 dB in two octaves. This filter provides a reasonable frequency response for the typical baseband filtering required for the project.

3.3.5 Resampling

The GC4016 receiver chip on the GC214 digital receiver contains a resampler that is capable of resampling the baseband signal at rates up to half the input clock, which allows filtered baseband data to be clocked from the GC214 at an arbitrary rate. This feature is ideal for a system that requires a specific data rate. It does, however, introduce some time latency into the signal path through the digital receiver. To avoid this added latency in the digital receiver, the resampler is not used. All of the output data rate control is implemented in the CIC decimation stage.

3.3.6 GC214 Latency

The data latency in GC4016 is calculated using the following formula. This is a delay from the rising edge of the step function as it enters the chip to the rising edge of the step function as it leaves the chip. An overall estimate of the latency through the chip, expressed in terms of number of input clock cycles is represented by the equation (35)

Total latency = (CIC latency = 2.5*N) + (CFIR latency = 0.5*N*CTAP) + (PFIR latency = N*PTAP) + (Resampler latency = 2*N*NMULT) + (Output delay) + (Pipeline Delay), (35)

where N = CIC decimation = 54, CTAP = 21, PTAP = 63. The total latency comes out to be 5010 clock cycles, and has been accounted for in the signal processing code.

3.3.7 Gain

Each of the receiver channels has two stages of gain control. One stage, which offers coarse gain control, is a simple bit shifter that provides gain factors that are multiples of 2. The

other stage provides fine gain control from a factor of 0.001 to a factor of 16. These gain stages are designed to allow gain compensation for the filtering stages. In the receiver driver, there is an algorithm that calculates the digital gain in the filter stages and then adjusts the coarse and fine gain control registers to provide a fixed gain through the digital receiver.

3.3.8 Data Header Format

All the four channels in the receiver are configured for continuous data collection after an external sync signal. In this collection mode, data are collected continuously after the receipt of rising edge of the external sync signal, and stored in sample FIFO memory in frames. The frame size was arbitrarily chosen to be 20400 samples in my code. The data frame header format containing a 16 bit frame counter, 16 bit channel ID, and a 32 bit timestamp was chosen. This timestamp register stores the number of clock cycles since it was last reset.

3.3.9 Direct Memory Access (DMA)

A PLX PCI9080 interface chip controls the two direct memory access (DMA) channels with two DMA transfer complete interrupt bits. DMA controllers must be programmed to use them for data collection. There are two modes of operation, chaining and non-chaining. We use non-chaining mode for our application. In non-chaining mode, the routine first initializes PLX PCI9080, which takes the local address of FIFO for a given channel, number of bytes to be transferred, and the physical address of DMA buffer created, as inputs. Once the initialization is done, it starts a data transfer and waits until transfer complete interrupt is enabled, and then aborts the transfer. It also checks for the elapsed time of the DMA transfer and if it does not complete in an acceptable amount of time it aborts. This prevents FIFO from acknowledging the local bus and thus prevents it from getting locked up.

3.3.10 DMA Buffer Creation

DMA by a device into the computer's RAM requires a physically and logically contiguous memory space. Hence we needed a routine that allocates a memory segment that is

physically contiguous and then memory maps that memory segment into the driver program, which makes it logically contiguous so that the code could use it as a normal pointer [15].

In the current GC214 driver code a function called "dma_alloc" (described in QNX memory documentation), has been used to create DMA buffers, and it essentially follows the procedure explained above. This function defines a structure named dma_t with segment number, length, physical and virtual address as its variables. This function takes a pointer variable of type dma_t and number of bytes, as inputs, and uses the "QNX_segment_alloc_flags" function to check whether memory segment is physically contiguous. This memory space is mapped into physical memory using "mmap" function, which essentially makes the address logically contiguous. The data written to a physical address actually could be accessed at a virtual address pointer.

These buffers act as any other buffer created by "malloc." I used these buffers in signal processing code as the malloc function failed to allocate huge chunks of memory. The "dma_ abort" function takes a pointer variable of type dma_t and uses "qnx _segment _free" and "munmap" functions to free the allocated buffers.

3.4 RAM-Disk

The GC214 stores received samples in a FIFO buffer, which extends up to 128K x 32 for each receiver channel, accounting for about 512K x 32 overall FIFO memory space. At a data rate of 300 kHz, the FIFO gets filled up in roughly 0.42 s. In order to assure no loss of data, the data need to be read at a faster rate from the FIFO, and stored in some physical storage device so they can be used for processing. It was observed that at such high data rates, streamlining data by writing them to hard disk was not ideal, as writing to hard disk was a slow process and couldn't keep up with the FIFO fill up rate. Hence, to get improved performance, a RAM-disk was created. QNX supports a file system in main memory called a RAM-disk. A RAM-disk is a block of memory that's accessed by the system as if it were a disk drive. It can be effectively used for temporary files or to augment the cache by storing frequently used data, such as programs or tables. Only one RAM-disk is supported by each Filesystem Manager (Fsys) process. The Fsys provides a standardized means of storing and

accessing data on disk subsystems. Fsys is responsible for handling all requests to open, close, read, and write to files. The following command was used to create a RAM-disk of 130 MB:

FSYS –NFSYSRAM –c0 –r130M

The options mentioned in the command used were not included in the QNX official manual. I got this from one of the online help forums. At one point playing with the sysinit file resulted in a system breakdown and the whole operating system was re-loaded.

Many other message passing techniques could have been used instead of RAM-disk, but they would have further complicated the system. I found RAM-disk was the most convenient and relatively simple means of data streamlining.

3.5 External Trigger Synchronization

The parallel port of the computer was configured to provide an external trigger to both the GC214 and the clock card. The pulse sequence generated from the parallel port has a 50% duty cycle and pulse frequency of 416.6 kHz, and a pulse width of 1.2 μs. The rise time of the pulse is negligibly small (< 0.1 μs), which is ideal for my application as long rise time might have caused added latencies. Whenever an external trigger needs to be given a function called "ext_trigger" is called, which forces the parallel port of the computer to generate a single pulse with the above mentioned characteristics.

The GC214 was configured to start data collection at an external trigger. In order to time synchronize the transmitter and receiver, as we said earlier, we use the clock card, which has been configured to get a timestamp of GPS time at an external trigger. The main driver code continuously reads the current GPS time and, at the 36^{th} second after every minute boundary, forces the parallel port to supply a pulse which acts as an external trigger to both the clock card and the receiver card. At this trigger, the receiver card starts collecting samples and the clock card time stamps the start time of data collection.

3.6 Signal Processing Code

Once data have been collected and stored in the RAM-disk, the signal processing code comes into the picture. The steps followed by the signal processing code are illustrated in the flow chart shown in Figure 3.9. The signal processing code reads ~116 MB of data from all the four channels and detects the pulse sequence initially by using a threshold detection algorithm. The detected pulse sequence is passed through two stages of correlation filters in order to precisely calculate the pulse's rising the edge sample number, then calculates the time from sample number and spits out files containing timestamps of the received pulse sequence. To illustrate and validate the results of the code written in C, a similar code was written in Matlab. The plots shown below are results obtained from Matlab code, which simulates the code written in C.

The signal processing code first picks a channel and does the processing and the repeats the same procedure for other the three channels. As each channel contributes about 29 MB of contiguous data, the signal processing code slides a window of length 20400 samples through the contiguous data and looks for the tail of a seven pulse sequence. There is a logical threshold setting routine that calculates the mean and standard deviation of given data (for every window) and sets the threshold depending on the signal strength. Versatile functions to calculate means and standard deviations were written based on standard formulae. After examining the threshold crossings the code recognizes the occurrence of a pulse sequence in the data set.

If we look at the radar generated pulse sequenc, which is shown in Figure 3.3, the last two pulses in the pulse sequence are separated by the unit fundamental pulse separation period. The signal processing code searches for the last two pulses of a pulse sequence by examining the pulse separation periods, and identifies them using the above mentioned, unique pulse separation period criteria.

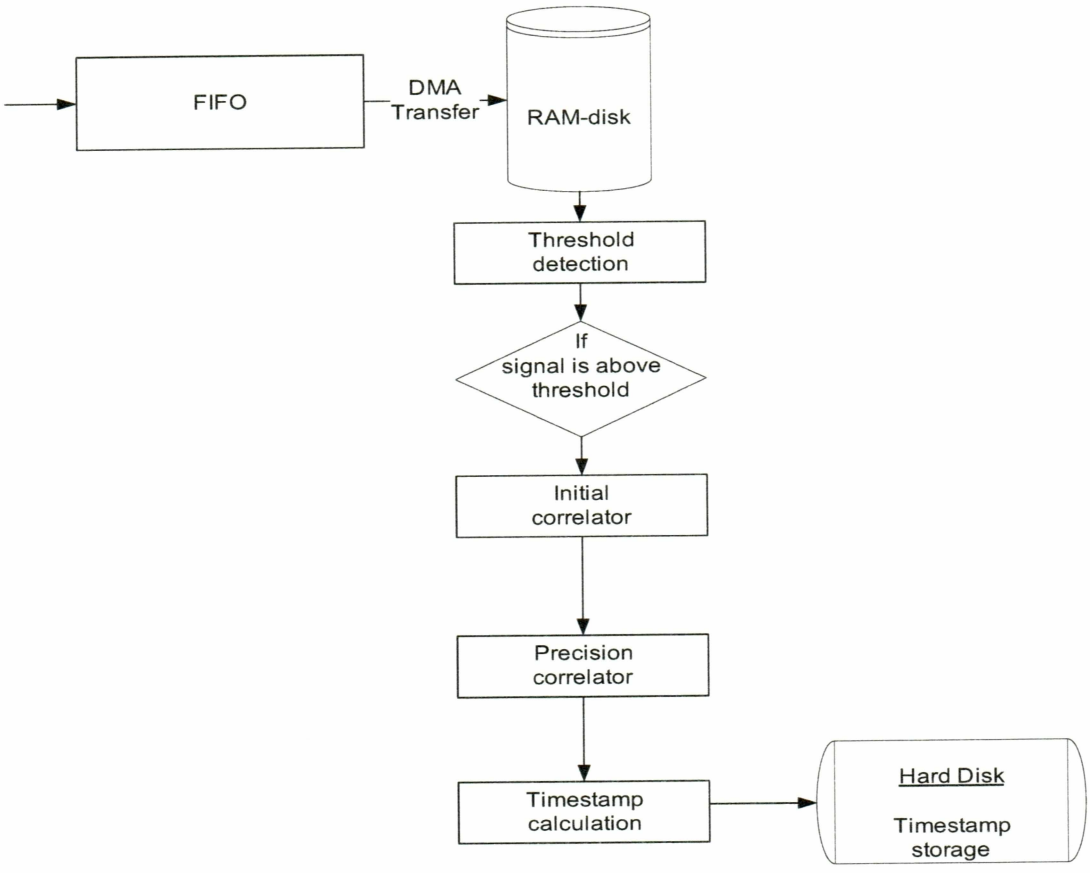

Figure 3.9 Figure Showing the Signal Processing Code Flow.

The following pictures depict the sequence of steps followed by the signal processing code. As mentioned earlier, these plots are generated by a signal processing code written in Matlab, for the data collected on March 15, 2005. Figure 3.10 shows the power plot of the samples collected. One can observe that the 7 pulses in a pulse sequence show up, but in two different windows as we limit our window size to 20400 samples. First 5 pulses occur in window 1, and the remaining 2 pulses from the same pulse sequence occur in window 2. The signal processing code initially confirms the presence of a pulse sequence by testing data with the threshold detection test, picks the pulses of the same sequence from two windows, and assimilates them into a single pulse sequence, as shown in Figure 3.11.

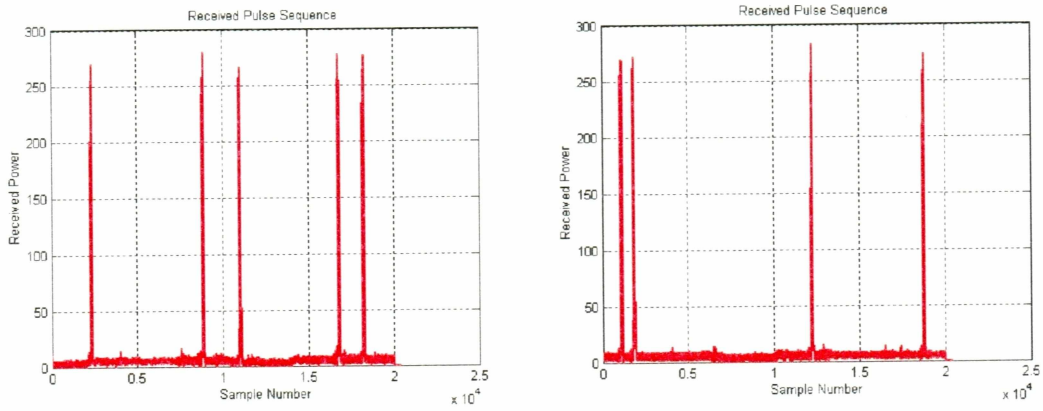

Figure 3.10 Window 1 Showing the First 5 Pulses and Window 2 Showing the Last 2 Pulses in the Same Sequence.

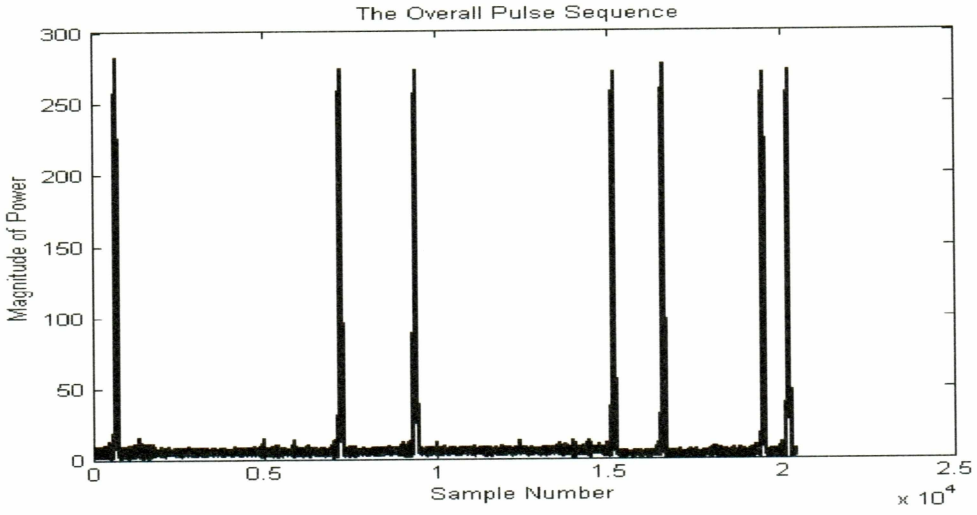

Figure 3.11 Assimilated Pulse Sequence.

This assimilated sequence is then correlated with the reference pulse sequence as shown in Figure 3.12.

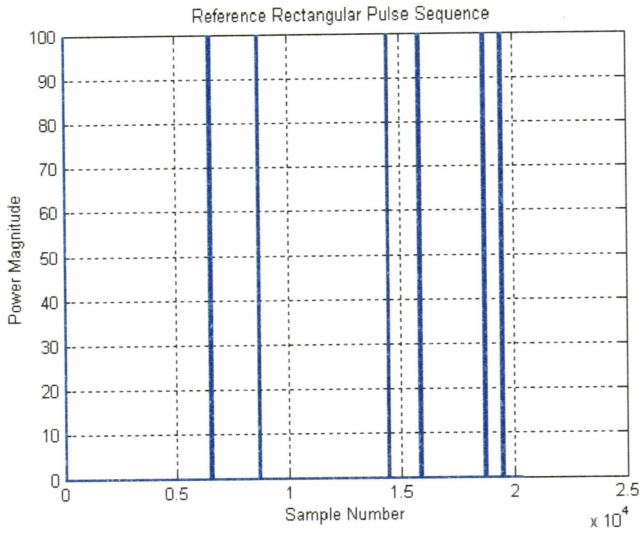

Figure 3.12 Reference Pulse Sequence Generated by the Computer.

This would give a rough estimate of the start of the pulse sequence. The plot of correlation for unit lag increments is shown in Figure 3.13.

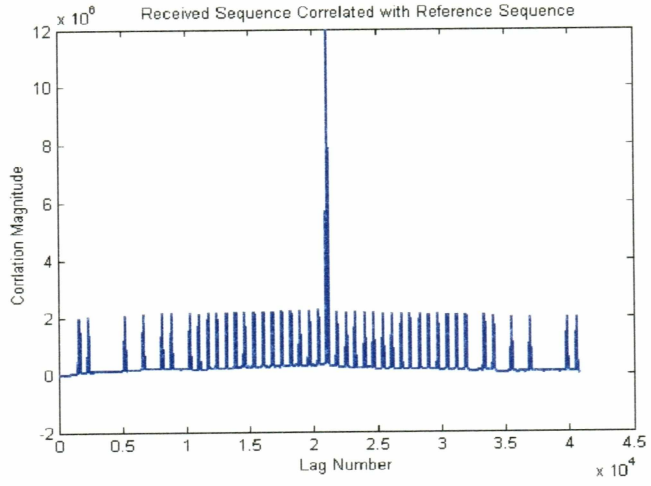

Figure 3.13 Plot Showing the Correlation Result of the Simulated Pulse Sequence and Received Pulse Sequence.

A simple correlation function, "x_corr," was written, which multiplies the time shifted version of one of the series with the other at different lags. The function takes the series to be

correlated and length of series as inputs, and gives the pointer to the correlated series as the output. As this correlation function had to perform numerous multiplications and additions to find coefficients at all lags, it took nearly 3.4 s to compute one correlation for a data set containing 20400 samples (window size). This time was long, as overall signal processing should take not more than 36 s, so that all the processing could be completed within one scan period. Hence a new function called "dec_seq" was written which decimates a given series by a given variable number of times. When a sequence that was decimated by a factor of 10 was correlated with the same length reference signal, the computation time was reduced to 0.1 s.

For the data under consideration, after initial correlation, sample number 651 was predicted to be the sample number of the rising edge of the first pulse in the pulse sequence. If we zoom into the first pulse in the pulse sequence shown in Figure 3.11, it can be observed that the code's prediction is off by few samples. Figure 3.14 shows the first pulse from Figure 3.11, on an expanded scale.

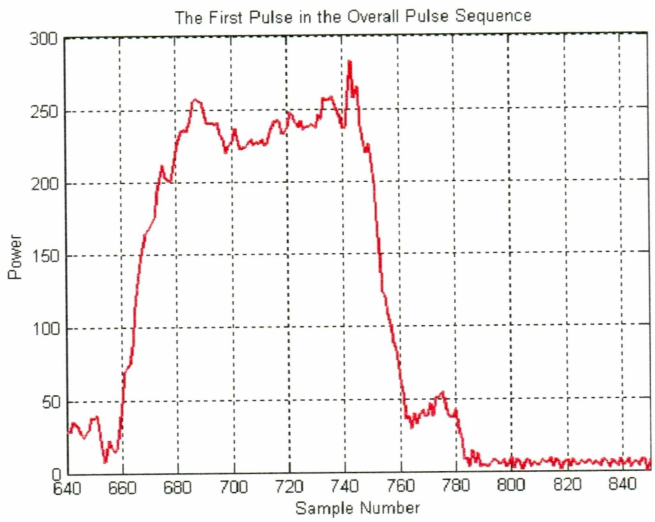

Figure 3.14 First Pulse in the Pulse Sequence Obtained.

In order to increase the accuracy in the pulse's rising edge sample number prediction, the code zooms into the location predicted by the initial correlation and traps a whole pulse, as shown in Figure 3.15. This pulse is again correlated with a hardwired expected pulse shape as

shown in Figure 3.16. This is considered the expected pulse shape as it resembles the shape of a rectangular pulse passed through a 22 kHz (radar signal bandwidth) low pass filter with added noise.

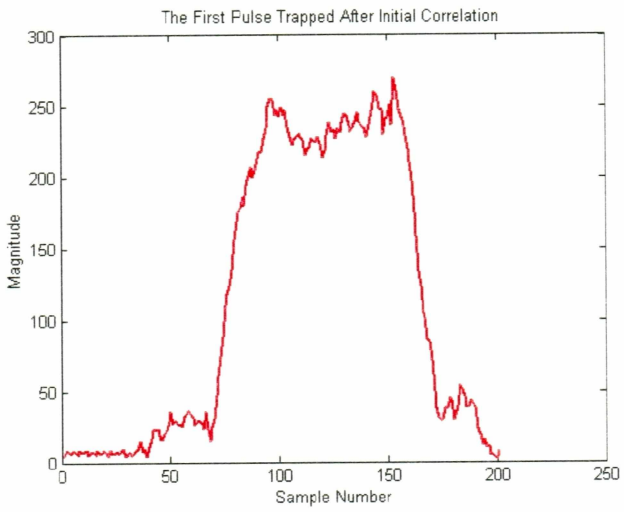

Figure 3.15 The First Pulse Trapped After Getting a Rough Index from Initial Correlation.

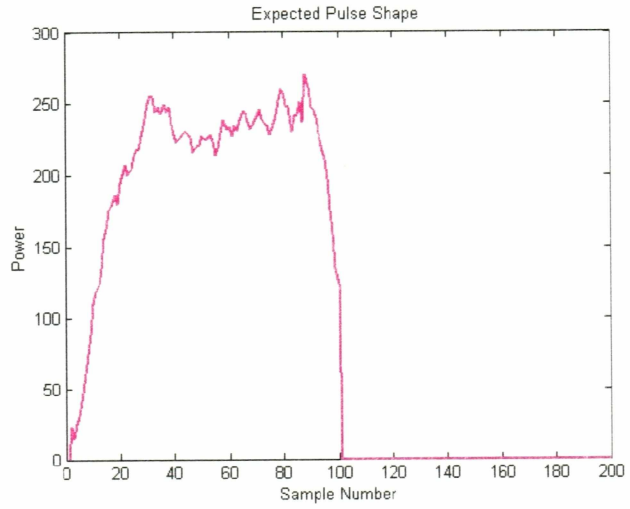

Figure 3.16 Expected Receive Pulse Shape.

The correlation peak as shown in Figure 3.17 occurs at the 68th sample, which when added to the initial correlation index gives the final sample number as 659. Hence the signal processing code finally predicts that the rising edge of the first pulse in the pulse sequence occurred at the 659th sample, which is shown in Figure 3.18.

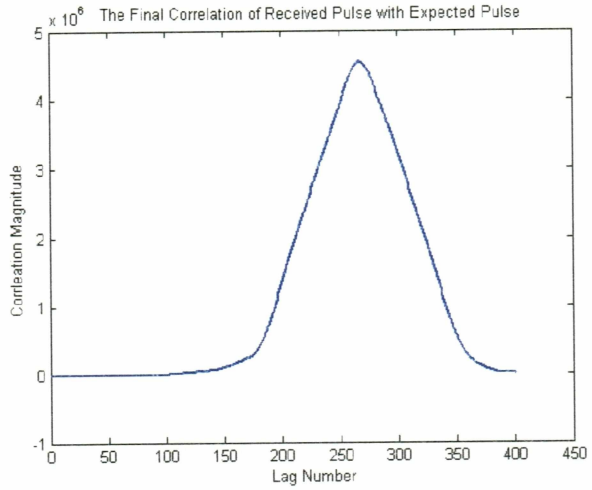

Figure 3.17 Final Correlation Plot.

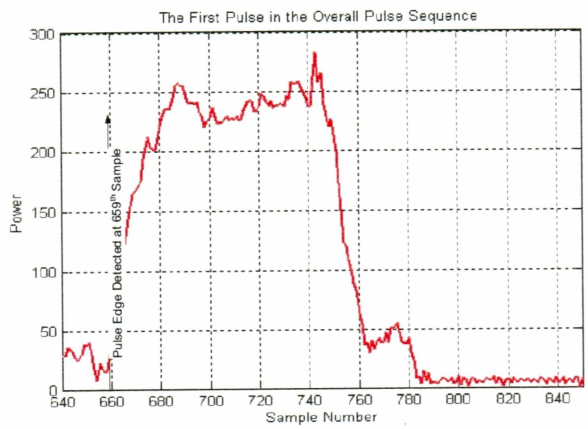

Figure 3.18 Plot Depicting the Rising Edge Sample as Detected by the Signal Processing Code.

Figure 3.19 shows the plots of another pulse and its rising edge sample number, as predicted by the code. Here the pulse edge was predicted to occur at the 654th sample.

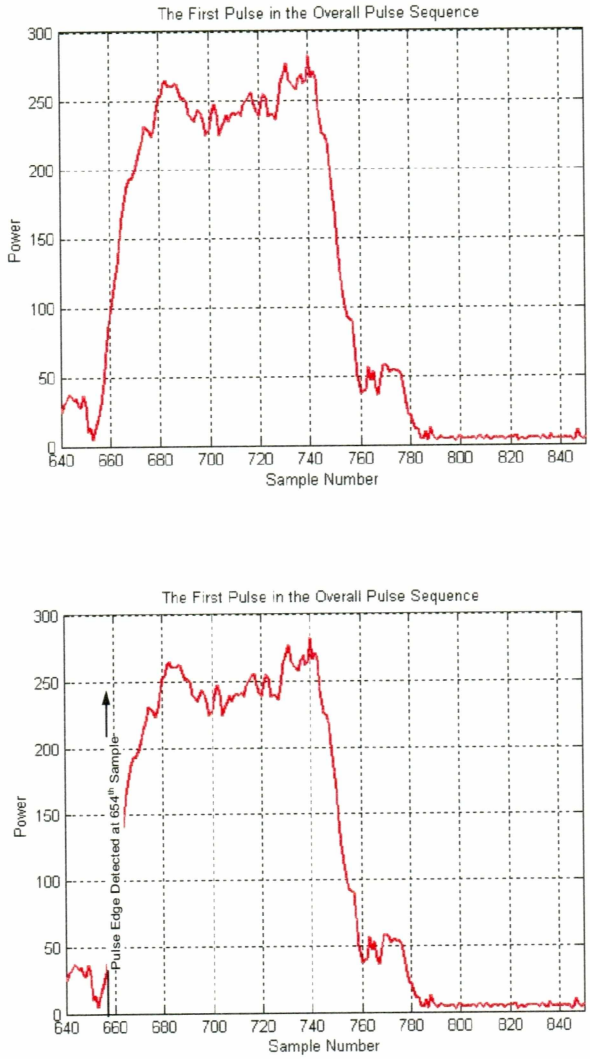

Figure 3.19 Plots Showing the Received Pulse and Predicted Pulse Edge Sample Number.

The same procedure is repeated for all the seven pulses in a sequence, and estimates of edge occurrence samples of each pulse in a pulse sequence are stored in a temporary buffer. In the end, the code again checks whether the exact sequence of seven pulses occurred or not

by cross checking the lags between the pulses. Only when all seven pulses satisfy the criteria of the fundamental pulse separation periods of a typical pulse sequence, as explained in Section 3.1, the code considers the sequence for time calculations.

The position of the window in which data occurred is tracked in the code and finally, following the above mentioned procedure, the position of a sample where a pulse edge occurred is determined with reference to the start of the whole data set. This is depicted in Figure 3.20. Here, say the rising edge occurred at the 658th sample in the 10th window from the start. The total number of samples from the start is calculated as 20400*9 + 658.

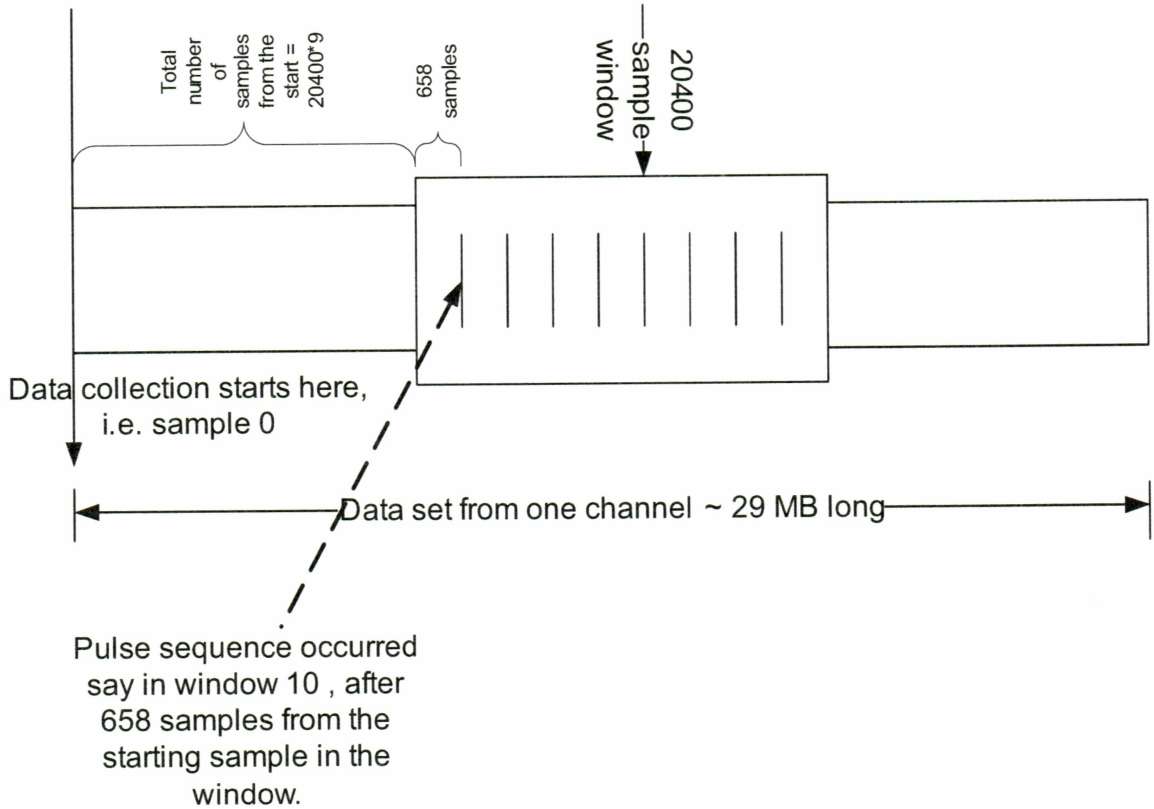

Figure 3.20 Picture Depicting the Sample Number Calculation from Reference.

Once the sample number of each pulse in a given data set for a channel is determined from the reference, multiplying the sample number with the inverse of sampling frequency gives the time of occurrence of the pulses. This time is added to GPS time obtained at the reference sample in the beginning and the final time of receipt of each pulse is calculated.

At this point, a few problems should be considered. The GC214 often failed to write a header for frame 0. Hence, to know the exact sample where the first sample with good data occurred became difficult. As a solution, frame 1 was considered as the reference point instead of frame 0. The signal processing code looks for the frame with frame count one and the typical channel ID. Then, to know the time of occurrence of frame 1 from the start, the timestamp register is read. This gives the number of clock cycles elapsed before frame 1 occurred. Dividing the clock cycles by clock frequency gives the time elapsed before frame 1 data are available. So all the sample numbers in a given data file are now calculated with reference to frame 1 instead of frame 0. This is depicted in Figure 3.21 and Figure 3.22, respectively.

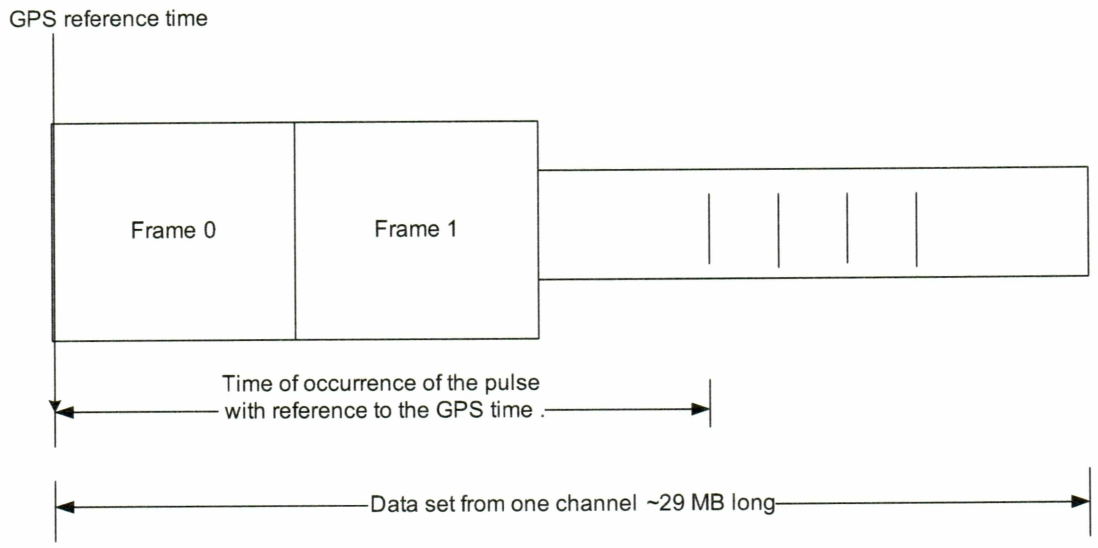

Figure 3.21 Diagram Showing the Initial Reference Location.

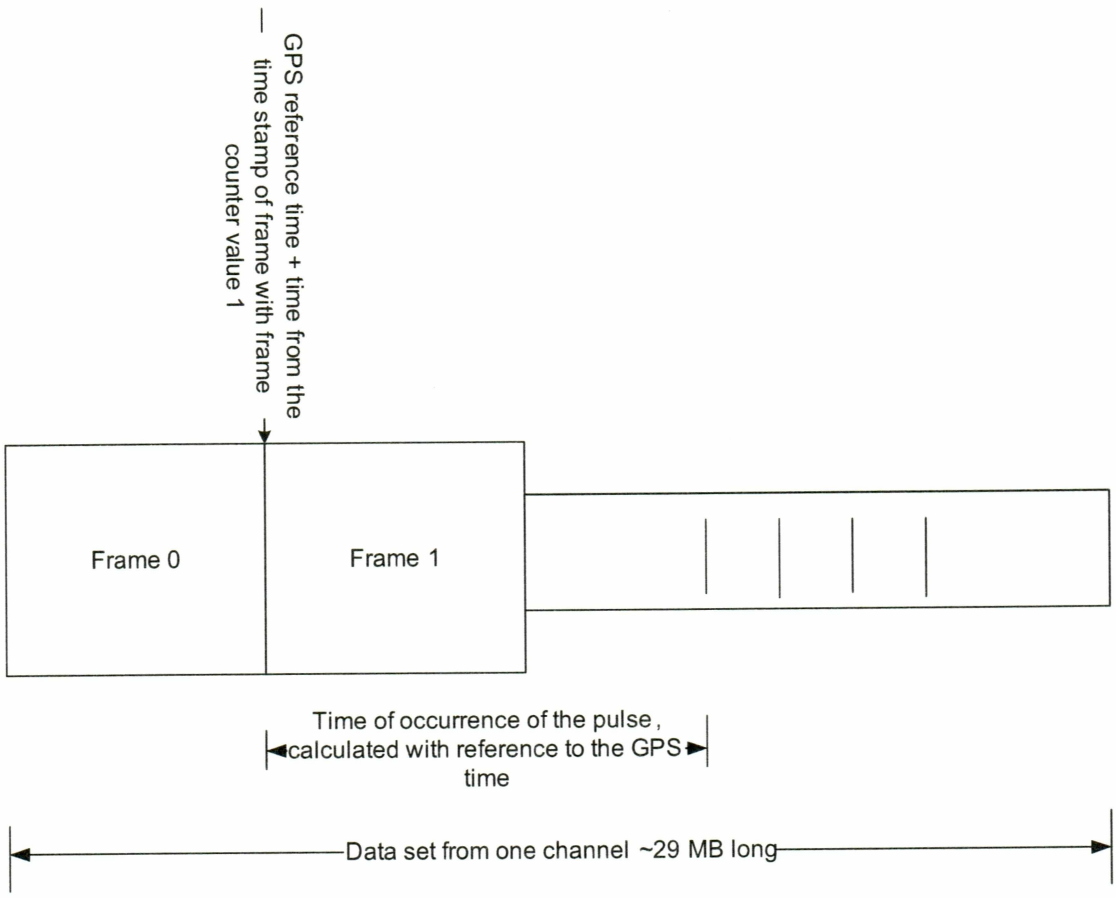

Figure 3.22 Diagram Showing the Final Reference Location.

The signal processing code calculates the time of arrival of each pulse from the reference point, as explained, above and adds it to the GPS reference time to get overall time and stores the time in seconds and nanoseconds since 1970 format. A counter in the code calculates the number of frames and number of headers to be subtracted from the sample count before calculating time. This is to neglect the header samples, as they cannot be considered as data samples. Also, the latencies in the card as explained earlier were taken care of.

In order to recognize the time stamp, the code generates a file name with the following format: "year-day-hour-minute-channel number-pulse sequence count." The task of

the signal processing code ends here and the overall driver code and the results will be discussed in the next chapter.

3.7 Link Budget

The signal-to-noise ratio for the receiving system was calculated to get a rough estimate of the received signal power that was expected. The receiving system consists of an antenna, coax cable and the receiver. The receiver is a cascade of an amplifier and the GC214 as shown in Figure 3.23.

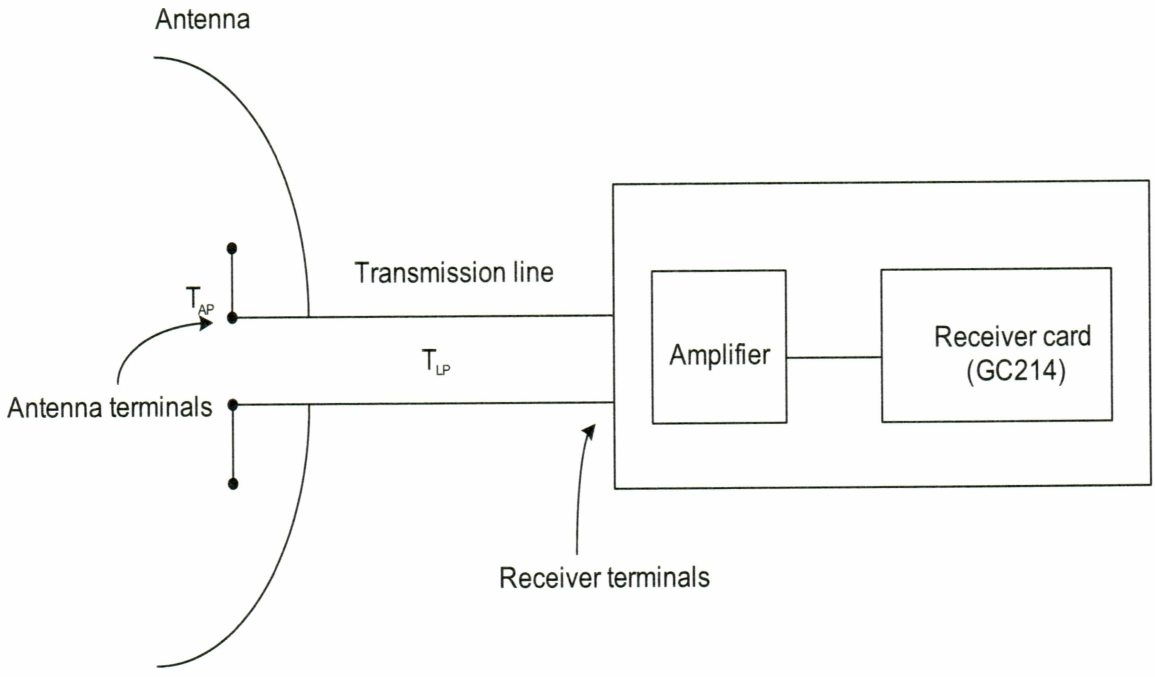

Figure 3.23 Block Diagram of the Receiver System [10].

The power received at the receiver (P_r) by a real antenna with an effective aperture area of A_e is given by equation (36), where P_t is the transmitted power, G_t is the gain of the

transmitting antenna, and R is the separation distance between the transmitter and the receiver [17]

$$P_r = \frac{P_t G_t A_e}{4\pi R^2}. \qquad (36)$$

The relation between gain and area of an antenna is

$$G_r = \frac{4\pi A_e}{\lambda^2}. \qquad (37)$$

The received power, shown in equation (38), is obtained by substituting equation (37) in equation (36)

$$P_r = P_t G_t G_r \left[\frac{\lambda}{4\pi R}\right]^2. \qquad (38)$$

Substituting G_t = 36.08 dB, P_t = 23.66 dBW (measured by Todd Parris, at 10.55 MHz), λ = 28.43 m, and R = 931 km (considering a reflection height of 155 km), G_r = 10.8 dB (obtained from the NEC model of a biconical corner reflector antenna at 10.5 MHz), we get a total received power of P_r = -41.7367 dBW. After taking into consideration the VSWR of the receiving antenna from Figure 2.17, cable loss of 2 dB/50 feet (specified by manufacturer), and gain through GC214, the net received power obtained is -47.5 dBW - 2 dB = -49.5 dBW. Here attenuation in the atmosphere was not taken into consideration.

The system temperature at the antenna terminals, as shown in Figure 3.23, is given by equation (39)

$$T_{SYS} = T_A + T_{AP} + T_{LP} + T_R, \qquad (39)$$

where T_A is the antenna noise temperature due to sky noise, T_{AP} is the antenna physical temperature, T_{LP} is the transmission line physical temperature, and T_R is the receiver noise temperature [17].

The receiver noise temperature for a cascaded system is given by equation (40)

$$T_R = T_1 + \frac{T_2}{G_1} + \ldots, \qquad (40)$$

where T_1, and T_2 are the noise temperatures of first and second stages respectively, and G_1 is the power gain of the first stage. The receiver temperature T_R is calculated by substituting T_1 = 412.09 K, G_1 = 126 (from manufacturer specifications), and T_2 = 300 K in equation (40). As the radar operates in the 8 to 20 MHz band, the T_A is of the order 10^4 K. Considering the ideal physical temperature of 300 K for the cable and antenna, the total system temperature, when calculated by using equation (39), equates to T_{SYS} = 11014 K.

The noise power of the receiver system is calculated using equation (41)

$$P_n = kT_{sys}B, \qquad (41)$$

where k = Boltzmann's constant = 1.38×10^{-23} J/K, B = bandwidth, which is 300 kHz in our case, and T_{SYS} is the system noise temperature = 11014 K. Hence, substituting these values in equation (41), we get a noise power value of -133.41 dBW. This results in an ideal signal to noise ratio of -49.5 + 133.41 = 83.91 dB, but the observed value of peak signal to noise ratio was ~28 dB.

Chapter 4. Results and Future Work

This chapter explains in brief the final code structure and displays the results that were obtained. A brief discussion of the validity of results and future work is also presented.

4.1 Final Code

The final code, which accomplishes the task of obtaining the timestamp of the rising edge of the received pulse, is the combination of the drivers for the clock card and the GC214, and the signal processing code. A robust code that collects and processes data continuously was developed. This code was loaded into the dedicated computer system sitting in a cabin near the receiving antenna at PFRR. The working of this code is explained in brief using the flow chart shown in Figure 4.1.

The clock card driver continuously monitors the current GPS time and waits for 36 s from a minute boundary. At the 36th second, the code forces the parallel port to generate a pulse which acts as synchronizing source to both the clock card and the GC214. The moment the GC214 receives an external trigger it starts collecting samples, and the GPS time at which this data collection started is registered by the clock card. The collected samples are DMA transferred from the GC214 FIFO to the RAM-disk. The signal processing code follows the steps explained in Chapter 3 and generates files containing the time of occurrence of the rising edges of pulses. This process is repeated for four different channels, and all the processing is completed in ~24 s. Then code waits until the 36th second from the next minute boundary and repeats the process, thus generating the received pulse times in real-time.

These files are read by a separate code and compared with the transmit end time stamp files, which are generated by the clock card driver on the transmitter end. The difference in time is fed to another piece of code which calculates the reflection height from the transmission time.

This project does not automate the file transfers and downloads and, hence, to validate the results, a one day worth of data was downloaded from both the transmit and receive ends

and time differences were generated and manually fed to the reflection height calculation code written in MATLAB.

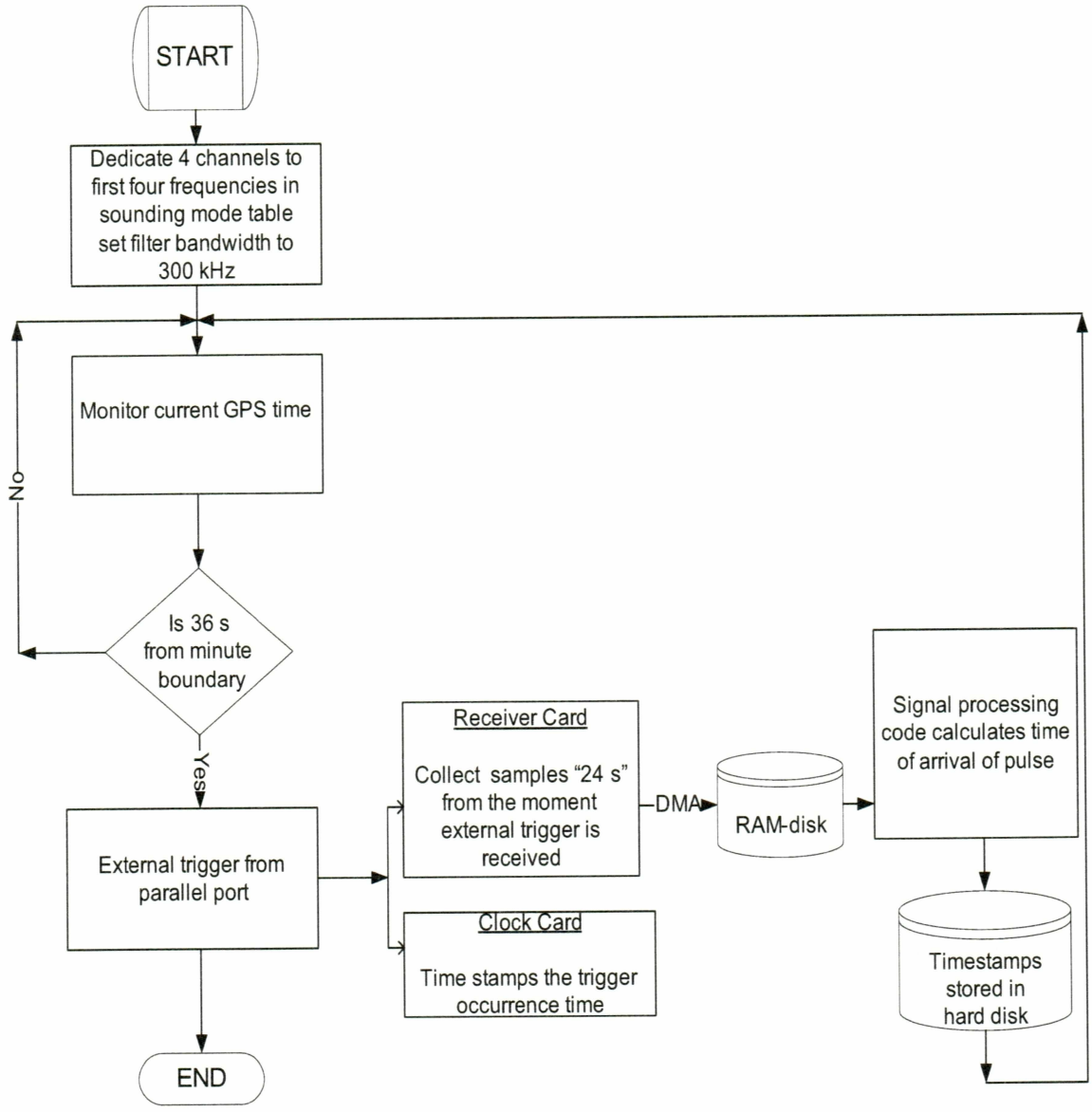

Figure 4.1 Flow Chart Explaining the Final Code Flow.

4.2 Results

The following plots show the reflection heights that were observed during the 24 hrs, starting from 01:00 hr UTC (5 PM Alaskan standard time) 30th April 2005 and ending at 01:00 hr UTC 1st May 2005. Pulse occurrence times were collected by the system sitting at PFRR. The overall reflection height for this day is shown in Figure 4.2. The reflection height in kilometers is plotted with respect to time in UTC. The four different frequencies are represented by four different colors as shown in the legend. The reflection heights shown by the plot vary from 140 to 170 km. The absence of sufficient ionospheric electron density to refract signals to the ground at night (04 hr to 12 hr UTC) is evident from the lack of many data points during that time. At a given time of day the reflection height increases with the increase in frequency. This trend is clearly displayed in Figure 4.3, which is an expanded version of the Figure 4.2. As expected, the ground scatter from the lowest frequency of 10.55 MHz is predominant, and accounts for the majority of reflection height points. The fact that the PFRR falls within the skip distance of higher frequencies is evident from the relatively lower number of reflection height points obtained from the highest frequency of 13.55 MHz.

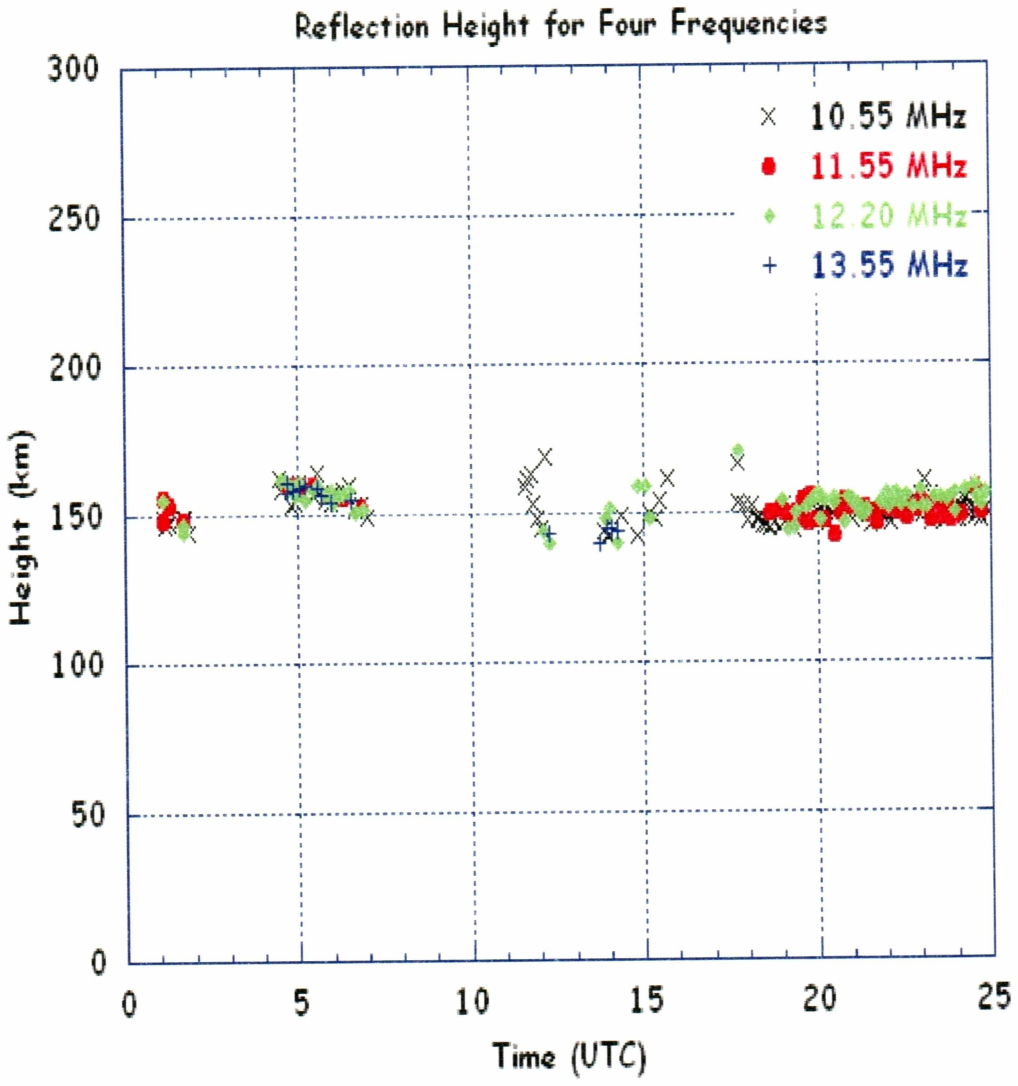

Figure 4.2 Reflection Height Plot for the Day - 30th April 2005.

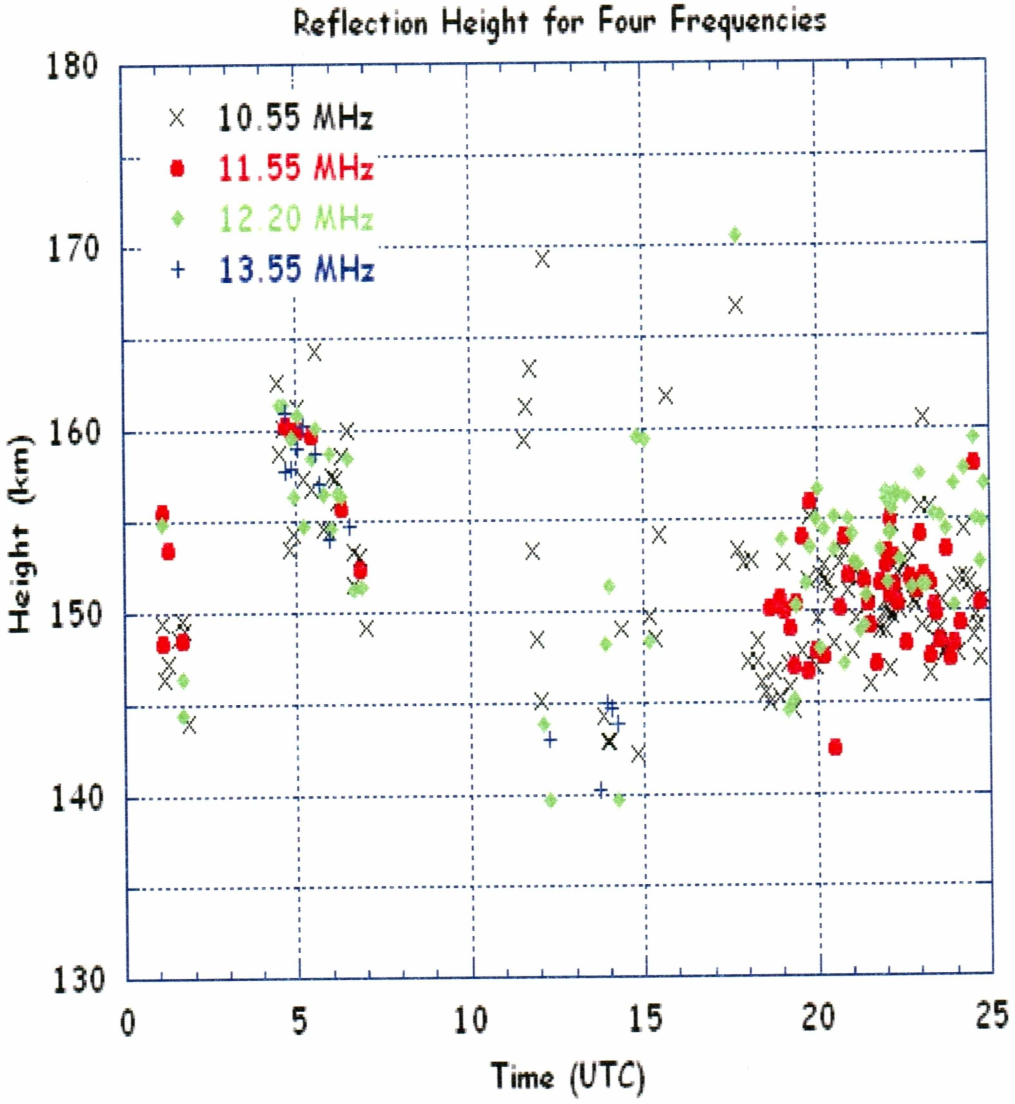

Figure 4.3 Reflection Height Plot Expanded.

The reflection height values were averaged over the 15 minute bins to reduce the variance. The plot shown in Figure 4.4 displays the mean data over each bin, illustrating trends more explicitly.

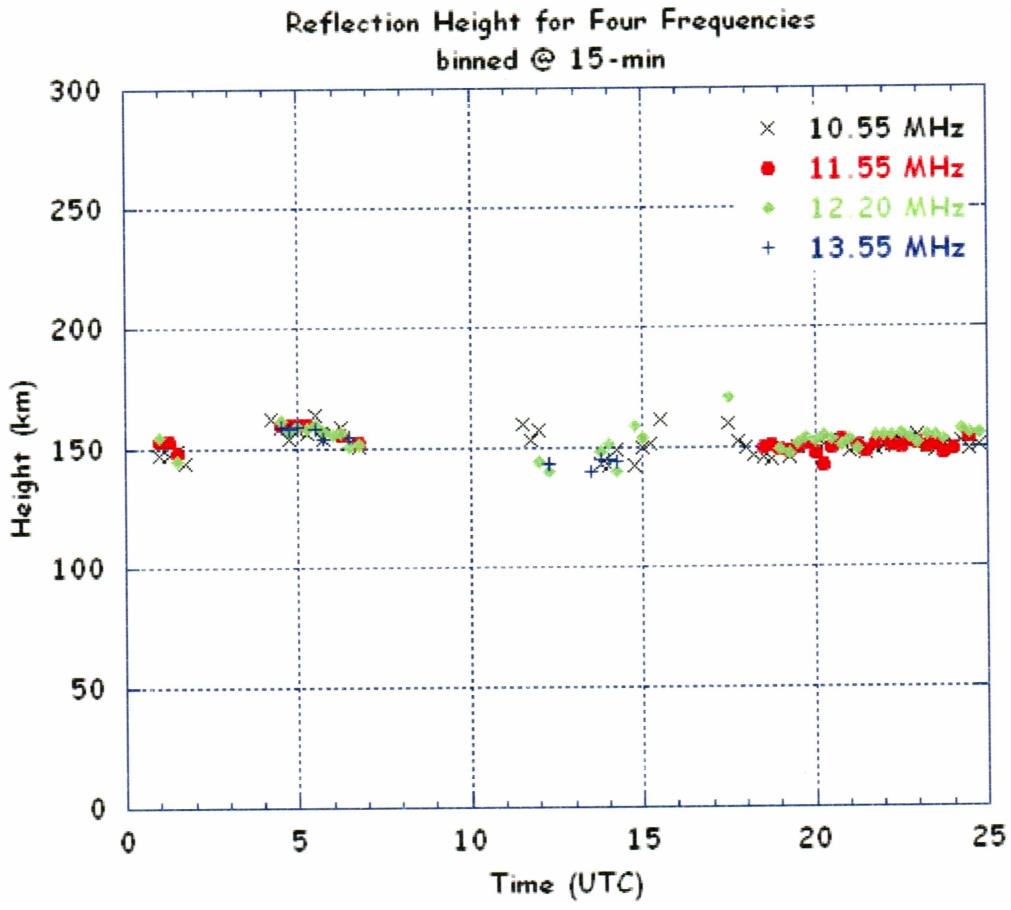

Figure 4.4 Reflection Height Averaged over 15 Minute Bins.

The reflection heights for four different frequencies averaged over 15 minute bins with error bars are shown in the following figures, from Figure 4.5 to Figure 4.9. The error depends on the number of sample points available in a given 15 minute bin. For the bins with good data, the error is not more than a couple of kilometers. But in a few cases the error bars are large, especially during night hours, when it is difficult to arrive at any conclusion looking at single day data. The concentration of data points from 20 to 24 hr is probably due to the presence of a strong E layer, which is validated by the SuperDARN ground scatter observation during that time.

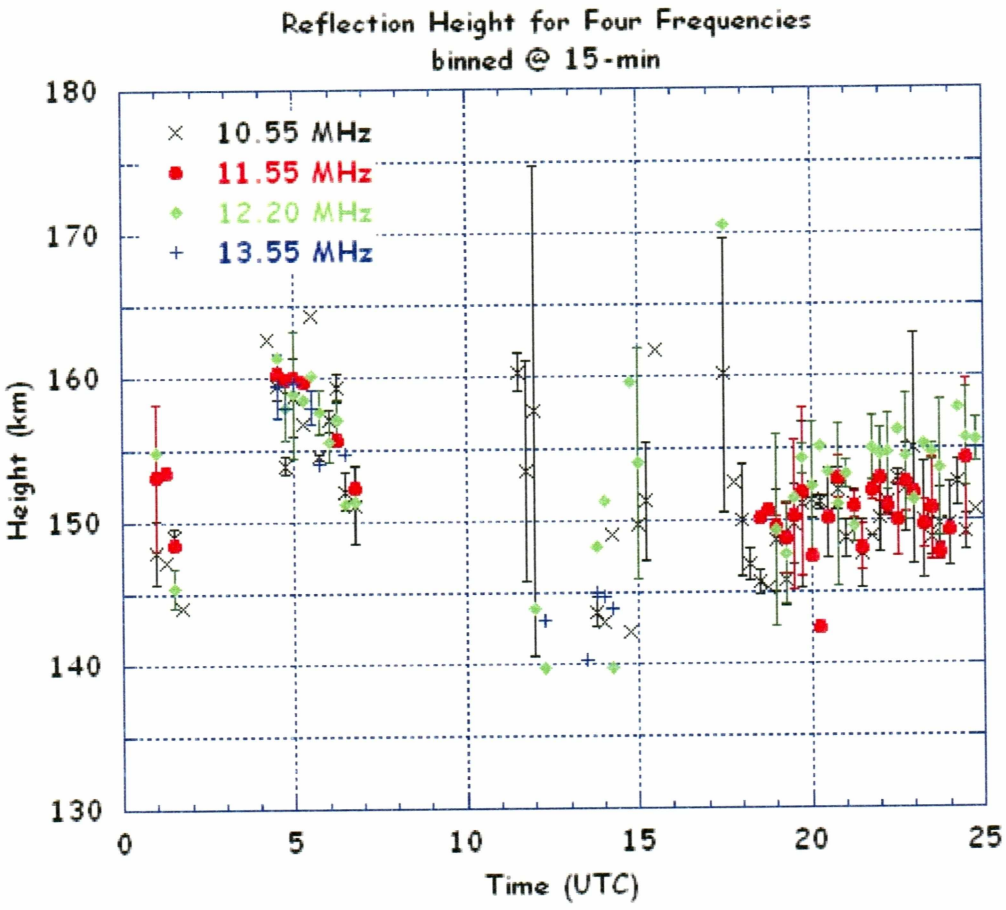

Figure 4.5 Reflection Height Plot with Error Bars for All Frequencies.

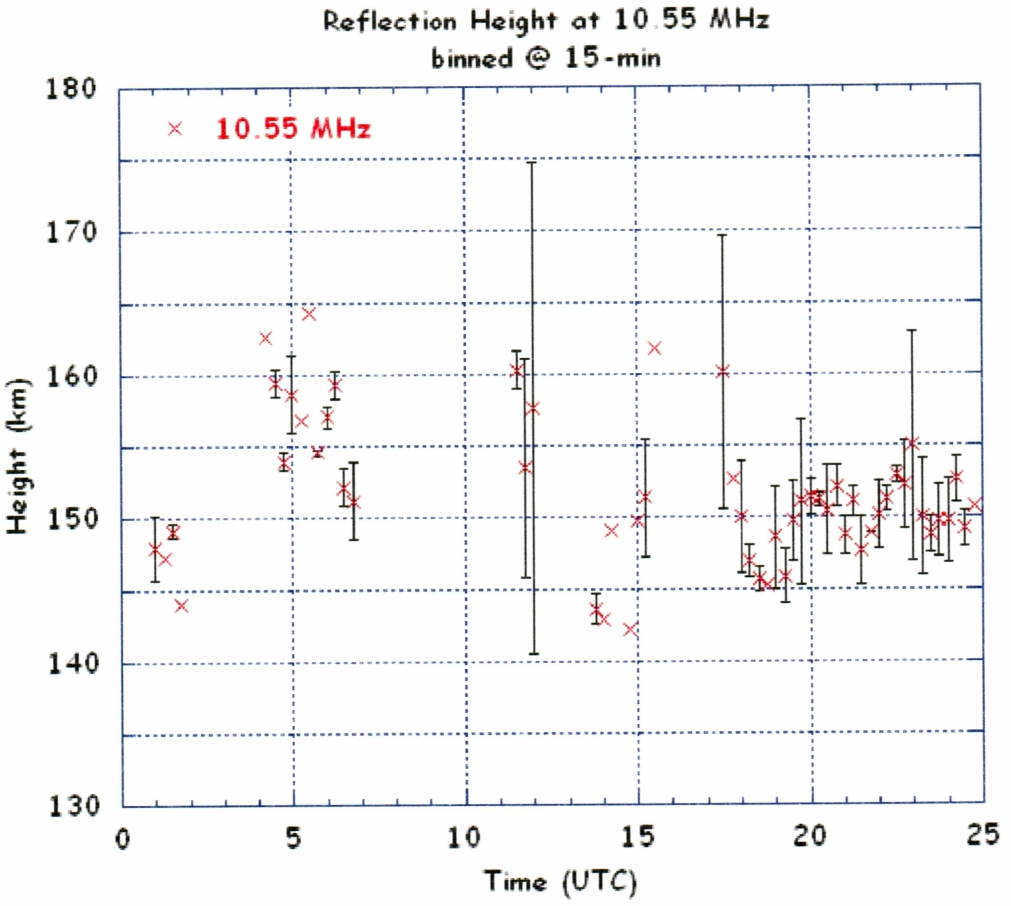

Figure 4.6 Reflection Height Plot with Error Bars for 10.55 MHz.

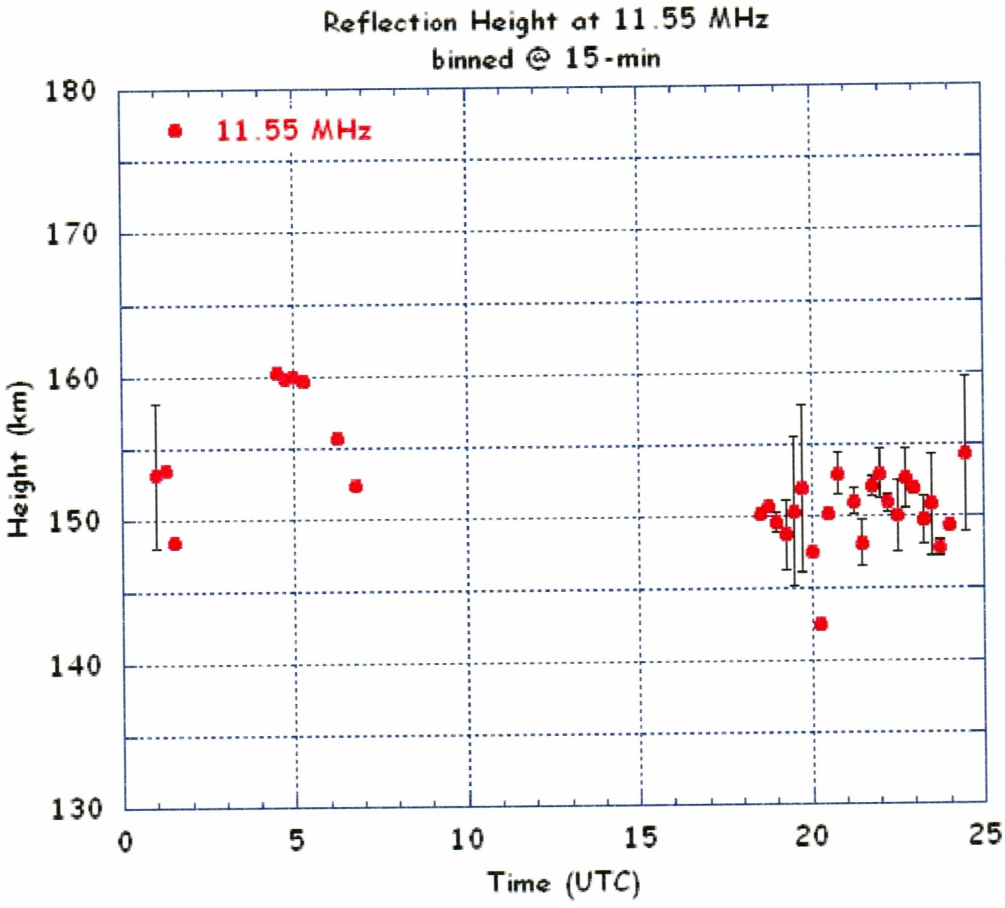

Figure 4.7 Reflection Height Plot with Error Bars for 11.55 MHz.

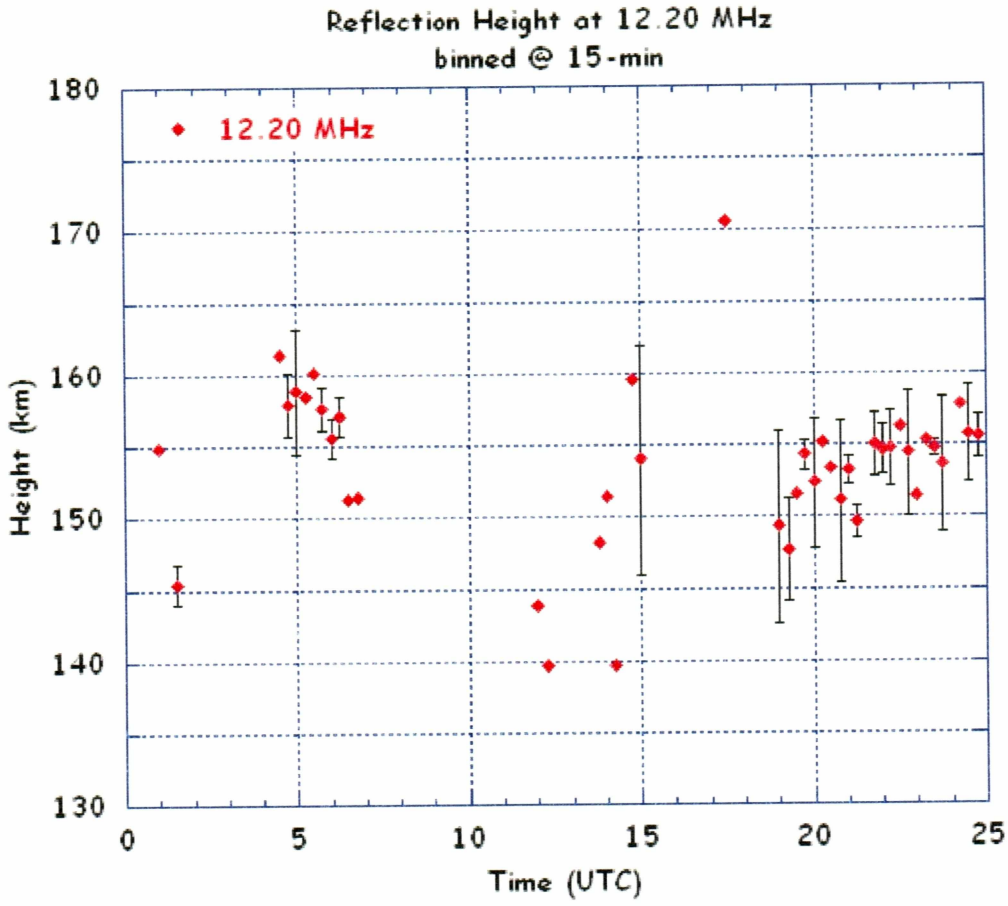

Figure 4.8 Reflection Height Plot with Error Bars for 12.20 MHz.

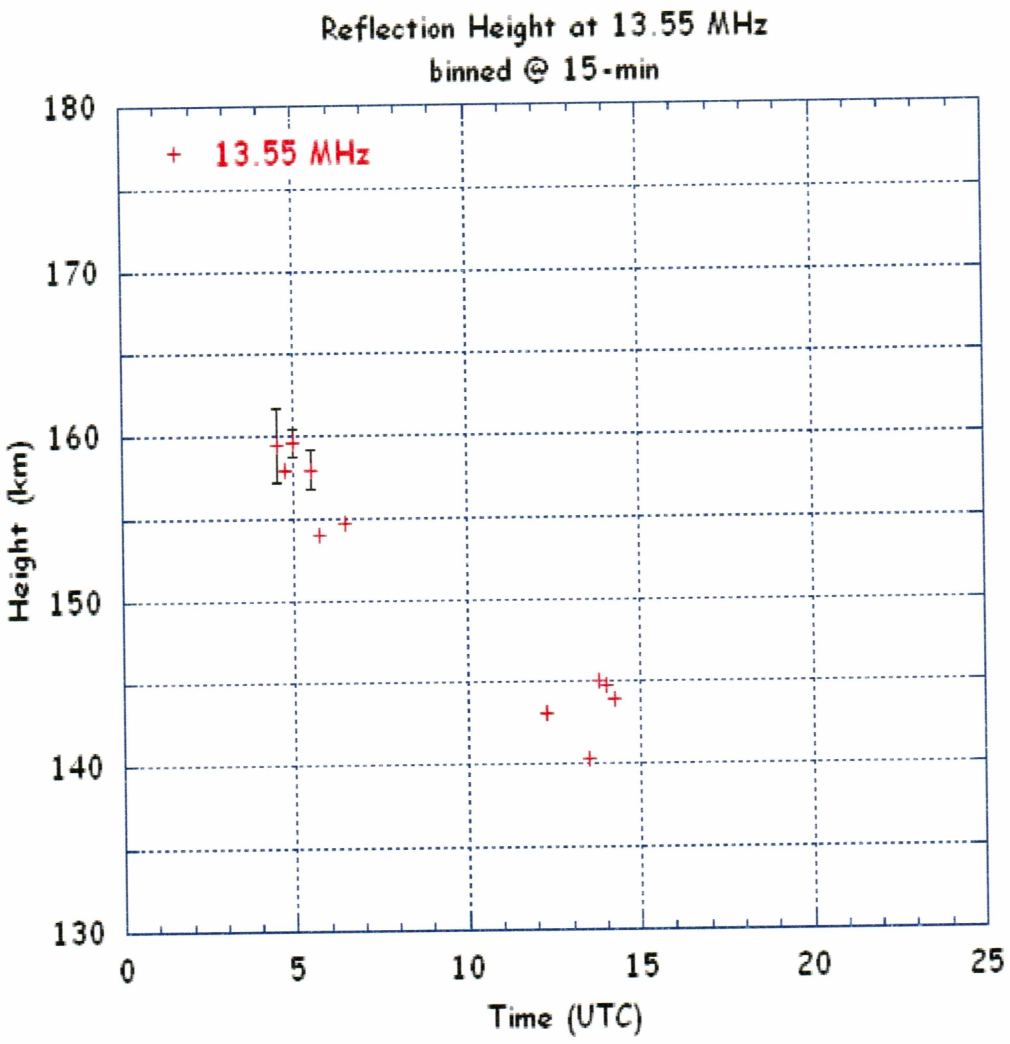

Figure 4.9 Reflection Height Plot with Error Bars for 13.55 MHz.

4.2.1 Errors

After a thorough analysis of error trends, it was observed that on an average there was a 2 μs increment in arrival times calculated for 100 ms time length when the signal processing was done assuming the clock frequency of 65 MHz. That is, estimates of the arrival times of each successive pulse group increased by 2 μs from those of the previous pulse group. Since the time was calculated by multiplying the sample number after the time reference by the

GC214 clock frequency, it was determined that the assumed clock frequency was incorrect, and is off by, $2\times10^{-6} * 65\times10^{6} / 100\times10^{-3} = 1.3$ kHz from the ideal 65 MHz.

After observing trends in data and adjusting the clock frequency of the signal processing code, we arrived at a conclusion that the actual clock frequency is 65001049 ± (0 to 40 Hz drift). This drift of 0 to 40 Hz was highly unpredictable, hence the frequency of the signal processing code was fixed at 65001049 Hz and the uncertainty in frequency prediction due to drift was accounted for as an error. This resulted in a maximum error of 14.7 μs (if we consider a maximum drift of 40 Hz) in a 24 s time set. This corresponds to a maximum error of 4.4 km in height prediction.

To reduce the error contribution from edge detection, the reflection heights from the seven pulses in a pulse sequence are averaged. The standard deviation of heights obtained from pulses within one sequence is in the range of mean height ± 0.6 km, which shows that the method predicts the reflection height accurately with worst case error being 5 km.

4.2.2 Applications

In the current critical frequency calculations using Kodiak SuperDARN data, the angle of arrival (AOA) of signal is calculated assuming a fixed reflection height ranging from 250 to 300 km. This results in error in critical frequency calculations. If the AOA estimations are made from the real-time reflection height data obtained, these errors could be significantly lowered.

4.3 Future work

Obtaining the reflection height data in real-time was the main target of this project, which has been almost accomplished, but with a few exceptions. The suggested future work includes developing an automated code in C that would communicate with the remote systems using reliable communication protocols and do the file transfer on its own. Then the time difference calculation and height calculation code bits should be assimilated to get the reflection height value in real-time.

In the edge detection code, a simulated rectangular pulse passed through a low-pass filter could be used as the hardwired pulse, instead of the pulse that is being used now. Adaptive magnitude pulse generation could be done to increase the signal detection accuracy while correlating. The drift in the clock frequency could be determined in real-time, which would further reduce the error in height calculations.

Bibliography

[1] M. P. M. Hall, L. W. Barclay, *Radio wave propagation-IEE electromagnetic wave series.* London, United Kingdom: Peter Peregrinus Ltd., 1989.

[2] K. D. Frogg, "The ionosphere explained." Internet: http://www.uaf.edu/asgp/hex/ionosphere.htm, [Mar. 10, 2005].

[3] R. D. Hunsucker, The high latitude ionosphere and its effects on radio propagation. New York: Cambridge University Press, 2003.

[4] Tony Hunt, "Ionospheric propagation explained." Internet: http://homepages.picknowl.com.au/wavetel/propagation.htm, Mar. 07, 2005 [Mar. 12, 2005].

[5] J. M. Hughes, W. A. Bristow, R. A. Greenwald, R. J. Barnes. "Determining characteristics of HF communications links using SuperDARN." *Annales Geophysicae*, vol 20, Mar. 2002, pp. 1023-1030.

[6] R. D. Hunsucker, *Radio techniques for probing the terrestrial ionosphere.* Berlin Heidelberg, New York: Springer-Verlag, 1991.

[7] Merrill Skolink, *Radar Handbook.* New York: McGraw-Hill, 1990.

[8] S. A. Hovanessian, *Radar system design and analysis.* Norwood, MA: Artech House Inc., 1984.

[9] R. T. Parris, "Design and implementation of a meteor tracking retrofit system for the HF radar at Kodiak Island, Alaska," M.S. thesis, Dept. Electrical. Eng., University of Alaska, Fairbanks, 2002.

[10] J. D. Kraus, R. J. Marhefka, *Antennas for all applications.* New York: McGraw-Hill, 2002.

[11] W. L. Stutzman, G. A. Thiele, *Antenna theory and design.* New York: J. Wiley, 1998.

[12] *Truetime model 560-5907/08 PCI-SG2 user manual*, Symmetricom, San Jose, CA.

[13] *Echotek ECDR-GC214-PCI/TS user manual*, Echotek Corporation, Huntsville, AL, 2001.

[14] Texas Instruments GC4016 multi-standard quad DCC chip data sheet, Palo Alto, CA, 2001.

[15] Frank Kolnick, *The QNX4 real-time operating system*. Canada: Basis Computer Systems Inc., 1998.

[16] Sanjit. K. Mitra, *Digital signal processing: A computer-based approach*. Boston: McGraw-Hill, 2001.

[17] Timothy Pratt, C. W. Bostian, *Satellite communications*. New York: J. Wiley, 2002.